



EU FP6-021285

CARDEQ

Carbon Nanotube Devices at the Quantum Limit

Specific Targeted Research or Innovation Project

FP6-2002-IST-C

D29: “Final Report”

Due date of deliverable: Month 42

Actual submission date: Month 42

Start date of project: 2006-03-01

Duration: 42 months

Organisation name of lead contractor for this deliverable:
Helsinki University of Technology (HUT)

Revision [1]

Project co-funded by the European Commission within the Sixth Framework Programme (2002-2006)		
Dissemination Level		
PU	Public	PU
PP	Restricted to other programme participants (including the Commission Services)	
RE	Restricted to a group specified by the consortium (including the Commission Services)	
CO	Confidential, only for members of the consortium (including the Commission Services)	

CONTENTS:

1	WP1 – Carbon nanotube FET	3
1.1	Summary	3
1.2	High mobility samples (Task 1.1, 1.3)	3
1.2.1	Shot noise from the Fabry-Pérot to the Kondo regimes	4
1.2.2	Shot noise in graphene strips	4
1.2.3	Theory of shot noise in nanotubes and graphene ribbons	5
1.3	High-frequency characterization (Task 1.4)	7
1.3.1	High-frequency characterization of NT-FETs	7
1.3.2	High-frequency characterization of GR-FETs	8
1.4	Optimization of Nano-FETs as pulsed charge detector (Task 1.2, 1.5)	8
1.4.1	Impedance matching of NT-FETs	8
1.4.2	Modeling of NT-FETs	8
1.4.3	Shot-noise limited sensitivity of NT-FETs	9
1.4.4	Theory of shot noise Schottky Barrier CNT-FETs	9
1.4.5	Single electron detection with NT-FETs	10
2	WP2 – Carbon nanotube rf-SET	11
2.1	Summary	11
2.2	Gate modulation (Task 2.2)	11
2.2.1	Fabry-Pérot regime and contact transparency	12
2.2.2	Kondo regime	13
2.2.3	Coulomb blockade regime	14
2.3	Sensitivity of carbon nanotube radio-frequency electrometers (Task 2.4)	14
2.3.1	Radio-frequency single-electron transistor	14
2.3.2	Radio-frequency resonant tunneling transistor	15
2.4	Electron-phonon coupling in nanotubes and graphene (Task 2.3)	16
2.4.1	Electron-phonon coupling in nanotubes	16
2.4.2	Electron-phonon coupling in graphene	17
3	WP3 – Control of the contact resistance	18
3.1	Summary	18
3.2	Normal metal contacts (Task 3.3)	19
3.3	Superconducting contacts (Task 3.4)	21
3.3.1	Single walled carbon nanotubes (SWCNT)	21
3.3.2	Multiwalled carbon nanotubes (MWCNT)	22
3.3.3	Renormalization of orbitals in superconducting electrodes	22
3.4	Cleaning by ion etching (Task 3.1)	24
3.5	Role of nanotube chirality (Task 3.2)	24
3.6	Integration of carbon nanotubes into semiconducting structures (Task 3.5)	25
3.7	Graphene	25
4	WP4 – Superconducting nanotube transistor	25
4.1	Summary	25
4.2	Induced superconductivity in multi-walled CNTs (Task 4.1)	26
4.3	Induced superconductivity in SWNTs (Task 4.2)	28
4.4	Induced supercurrents in graphene	30
4.5	Cooper-pair beam splitter using SWNTs (Task 4.3)	30
4.6	High-frequency properties of nanotube junctions (Task 4.4)	32
5	WP5 – Nanomechanical force sensor	33
5.1	Summary	33
5.2	Scanning force microscopy detection	33
5.3	Mass sensing	34
5.4	Coupling mechanical vibrations with charge transport	35
5.5	High-bandwidth detection scheme	36

1 WP1 – Carbon nanotube FET

1.1 Summary

The work of *WPI* has concentrated in understanding phenomena that affect RF transport dynamics and charge sensitivity in Nano-FET type of devices made of semi-conducting carbon nanotubes or semi-metallic graphene sheets. We have studied, both theoretically and experimentally, at room and cryogenic temperatures, the GHz operation of single wall nanotube FETs (NT-FETs) and single layer graphene FETs (GR-FETs). Measured transport parameters are i) the drain-source conductance g_d , ii) the transconductance g_m , iii) the gate capacitance C_g , iv) the transit frequency f_T and v) the shot noise S_I . In most cases we have provided the first GHz determination of these quantities and in some cases we have been able to compare quantitatively their absolute or relative values with theoretical predictions for the ultimate quantum limit, meeting thereby one of the main scopes of the CARDEQ project.

In particular, we have shown that NT-FETs constitute the paradigm of a 1-dimensional nano-transistor: the 4-mode ballistic Nano-FET. Our analysis points to the importance of hot electron effects in the 1-dimensional access leads to the gate, which limits sensitivity at cryogenic temperatures. This affects mainly noise which is thermal shot noise that can be alternatively described as $S_I = 2eIF$ using an apparent Fano factor $F \approx \coth(eV/2k_B T_e) \sim 1$ and DC current I , or as thermal noise $S_I = 4g_n k_B T_e$ in terms of a noise conductance g_n and the electronic temperature T_e . With $g_n \geq g_d$, this equation is a generalization of the Johnson-Nyquist expression to the case of multi-terminal active devices. We have provided the theoretical expression, $g_n = g_d + g_m/2\beta$, for the 1-dim Nano-FET model and verified its validity by measuring the rf noise at high bias in NT-FETs.

The charge sensitivity of a double-gated device, $\delta q \leq 13 \cdot 10^{-6} e/\text{Hz}^{1/2}$ at 4.2 K, has been measured in a broad $\Delta f = 0.8$ GHz bandwidth which corresponds to a sensitivity-bandwidth product of $\Delta f/\delta q \leq 6 \cdot 10^{13} \text{ Hz}^{3/2}/e$. This corresponds to an rms charge resolution of a $0.3e$ for a double gate device in the 0.2–0.8 GHz detection bandwidth or our experiment. This demonstration of nanosecond single electron resolution fulfils one part of the experimental goals of the CARDEQ project which was to demonstrate single electron detection in a single-shot nanosecond measurement.

The excellent dynamical properties of GR-FETs have been demonstrated at room temperature up to 1.6 GHz and 60 GHz at 77 K showing very high transconductance in excess of 1.5 mS/ μm . Transit frequencies as high as 15 GHz have been measured, and intrinsic transit frequencies of 35 GHz have been estimated on samples of lower mobility (0.5 mS/ μm). When put in perspective with the strong shot-noise suppression reported at low temperature, these results confirm the great potential of GR-FETs for low noise microwave application. Micro-GR-FETs promise to reach the important W-band (90 GHz) in the near future and their Nano variants may well surpass CNTs for cryogenic fast charge detection.

1.2 High mobility samples (Task 1.1, 1.3)

Nano-FETs used for fast charge detection have a typical gate length of 100 nanometers. Ballistic transport requires large mobility in the $10\,000 \text{ cm}^2/(\text{V}\cdot\text{s})$ range. These are accessible at room temperature in carbon-based devices thanks to the low mass and high velocity and the weak scattering of carriers. We have approached this goal using CVD grown nanotubes and graphene sheets and as well as exfoliated graphene flakes. We have also shown that these high performances are preserved in the presence of top-gates and best exploited by using low resistance Pd contacts. Finally we have shown that NT-FETs keep their unique properties in the RF frequency domain.

1.2.1 Shot noise from the Fabry-Pérot to the Kondo regimes

One way to assess the high quality of semiconducting nanotubes consists in measuring their low-bias noise properties at low temperature, in a regime where quantum coherence effects, which are very sensitive to residual scattering in the nanotube, become prominent. The nanotube plays the role of a quantum impurity with a tuneable transmission. Here we take advantage of the presence of Schottky barriers at the metal-semiconducting nanotube interface to realize a Schottky transistor controlled back gate. CVD nanotubes being naturally p-doped, the electronic transmission D is low at positive bias where Coulomb blockade diamonds are observed, high at negative bias with a characteristic Fabry-Pérot (FP) checker-board pattern with conductance maxima at $4e^2/h$. In the intermediate transmission regime Kondo resonances are observed with a unitary conductance of $2e^2/h$. We have been looking for signatures of ballistic transport in FP regime and interactions in the Kondo regime in the low-frequency shot noise. We have observed the (1-D) suppression of shot-noise at FP resonances and the resurgence of a shot-noise maximum at the Kondo resonances.¹ None of these results could have been observed in a diffusive nanotube.

1.2.2 Shot noise in graphene strips

Owing to its unique structure, graphene conduction occurs via massless Dirac fermions. Graphene is a gapless semiconductor: the conduction and the valence band are touching in two inequivalent points (K and K', usually called Dirac points) where the density of state vanishes. Nevertheless, the conductivity at the Dirac point remains finite as charge is carried by evanescent waves, i.e. by tunneling between the leads. These unique properties are also reflected in the shot noise properties of graphene. In perfect short and wide graphene strips ($W/L \geq 3$), for heavily doped graphene leads, at the Dirac point both minimum conductivity and Fano factor are expected to reach universal values of $4e^2/\pi h$ and $1/3$, respectively. Astonishingly, the transmission coefficients at the Dirac point in perfect graphene show similar form as those found in diffusive systems.

We have studied shot noise in short and large graphene strips (with different width over length ratio W/L) prepared by Prof. A. Morpurgo and his collaborators in Delft. The samples were made of graphene sheets exfoliated from natural graphite and deposited on top of Si/SiO₂ wafer, where the substrate is used as a back gate. Our measurements show that for strips with large W/L , both minimum conductivity and Fano factor reach universal values of $4e^2/\pi h$ and $1/3$, respectively. We find that the Fano factor has a maximum at the Dirac point and it diminishes with increasing carrier density. We also see that for smaller W/L ratios, the Fano factor is lowered as expected by the theory. While the ballistic nature of conduction in graphene is strongly debated, our findings support the view that transport at the Dirac point occurs via evanescent waves, i.e. that carriers can propagate without scattering.

¹ T. Delattre *et al.*, Nature Phys. **5**, 208 (2009).

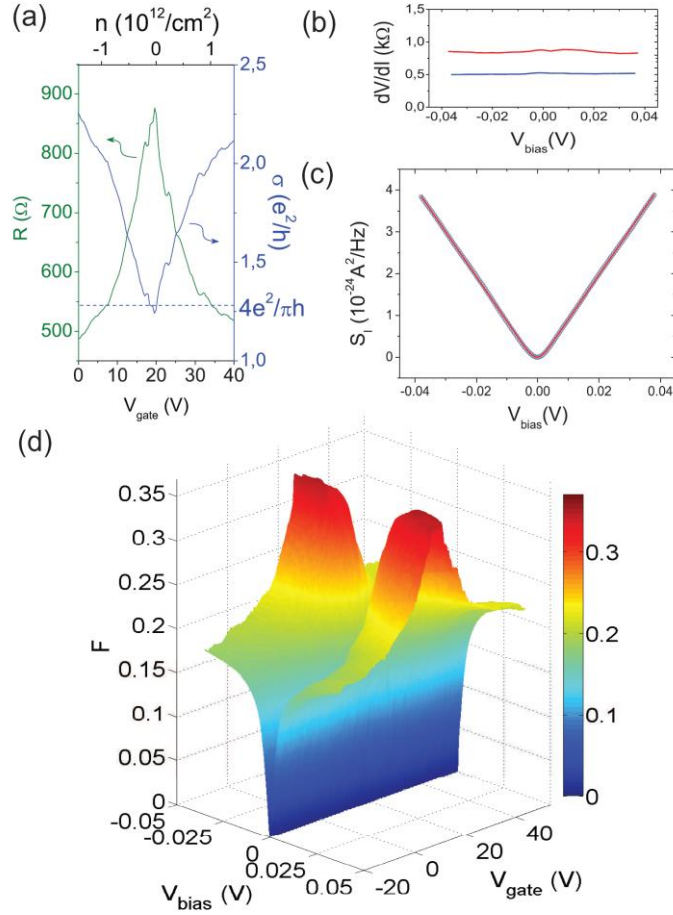
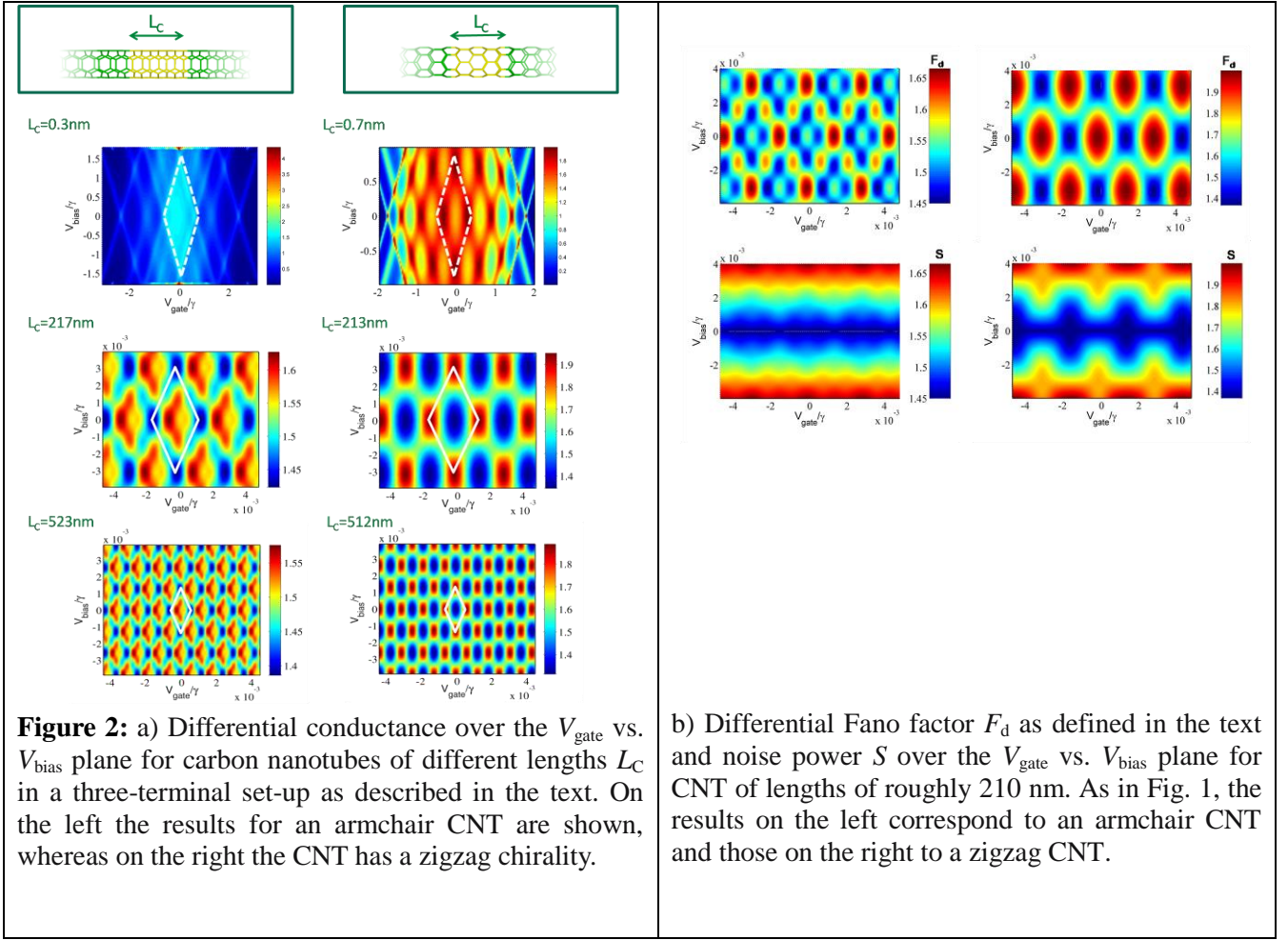


Figure 1: Measurements on sample with $W/L = 24$: (a) Resistance R (left axis) and conductivity σ (right axis) as a function of V_{gate} . (b) Differential resistance dV/dI versus bias voltage V_{bias} at the Dirac point (red curve) and at high density (blue curve). (c) Current noise per unit bandwidth S_I as a function of bias at the Dirac point, at $T = 8.5$ K, fitted (red curve) using Khlus formula ($F = 0.318$). Note that the low bias data are perfectly fitted as well as the high bias (d) Mapping of the average Fano factor F as a function of gate voltage V_{gate} and bias voltage V_{bias} at $T = 8.5$ K.

1.2.3 Theory of shot noise in nanotubes and graphene ribbons

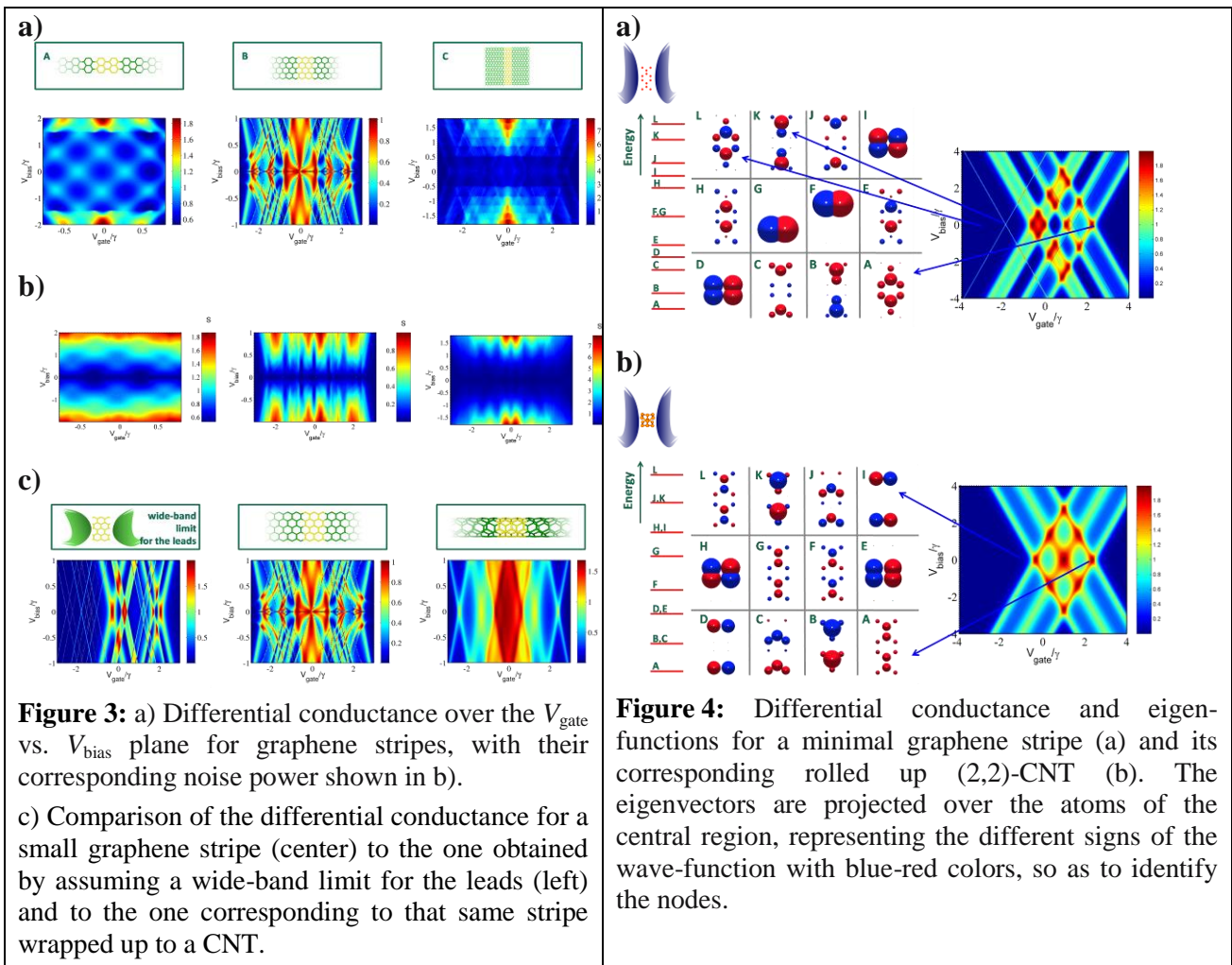
Following up our investigation of the transport properties in the Fabry-Pérot regime and the contact transparency, we have analyzed the differential conductance and shot noise power of carbon nanotubes (CNTs) and graphene stripes. We study these systems in three terminal set-ups, where a bias voltage is applied along the tube/stripe assuming a symmetrical voltage drop at the interfaces of the central region and the leads. A gate voltage provides an important mechanism to explore the states of the system and is applied to the central region. The leads are assumed to be of the same type as the central region, so that we would obtain perfect transparency for the CNT/stripe conductance, if we would not introduce barriers at the interfaces to the leads. The wide-band limit (no energy-dependence of the self-energies) is also considered for the leads.



We find the following results:

- As we can see in Figure 2a, the energy scales of the stability diagrams go inversely proportional to the length of the scattering region.
- In Figure 2b results for the shot noise and differential Fano factor are shown. The noise power modulates the Fano factor in an oscillatory behavior. Values larger than one are found for this factor as in experiments, though in our calculations even larger values are reached.
- Some results for graphene stripes are presented in Figure 3a-b. As made clear in the comparison of Figure 3c two conclusions can be drawn: on the one hand graphene ribbons present more complex stability diagrams and different energy scales are seen in the diamond patterns. There are remarkable differences between zigzag- and armchair-edged ribbons. We can see how the features on the stripes with zigzag edges deviate from the linear behavior characteristic of these stability diagrams. Work towards the understanding of this behavior is being carried out. On the other hand, the leads have a strong effect being responsible for symmetry-related suppression of transmission.
- By studying a very reduced scatterer of a (2,2)-CNT and its corresponding graphene ribbon used leads in the wide-band limit, we could analyze the distribution of the eigenchannels through the atoms. By focusing on the dark states (non-conducting, and thus not seen in the stability diagram) in the CNT which become conducting in graphene ribbons, one can see that the symmetry of these states changes from one to another due to the changed boundary conditions perpendicular to the transport axis. The open boundary conditions of graphene

ribbons result in new conducting channels that are present in the CNTs but which transmission is suppressed for symmetry-reasons.



1.3 High-frequency characterization (Task 1.4)

1.3.1 High-frequency characterization of NT-FETs

Our typical RF NT-FET layout, shown in the electron-beam micrograph below, consist of a symmetric double gate design (nanotube diameter $d \approx 1.5$ nm, channel length 1 μm , gate length 300 nm, oxide thickness 6 nm).

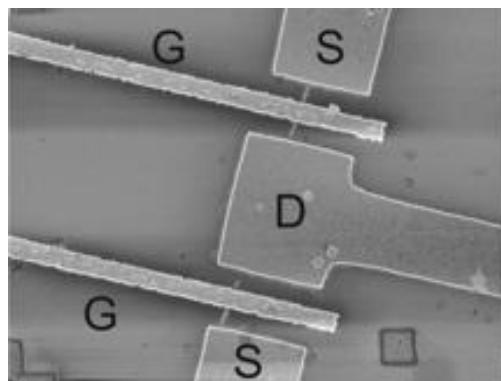


Figure 5: Scanning electron microscope image of a single carbon nanotube double-gate transistor. The gate length is 300 nm.

Gate-drain transmission measurements were performed at room temperature up to 1.6 GHz to deduce transconductance ($g_m \approx 20 \mu\text{S}$ at 0.5 V bias) and gate capacitance ($C_g \leq 30 \text{ aF}$). Due to their high impedance it is not possible to measure directly their f_T , which was estimated from the ratio $g_m/2\pi C_g \approx 50 \text{ GHz}$.

From measurements in long gate devices we deduced the carrier mobility $\mu = 3500 \text{ cm}^2/(\text{V}\cdot\text{s})$, and the gate coupling factor $\beta = C_g/C_q \approx 0.2$, where C_q is the quantum capacitance, which is an important parameter of the modeling.

1.3.2 High-frequency characterization of GR-FETs

The same technique was used to characterize graphene FETs (channel width 0.9-1.2 μm , channel length 300 nm, gate length 100 nm, oxide thickness 2 nm) with a mobility $\mu \approx 240 \text{ cm}^2/(\text{V}\cdot\text{s})$ and a transconductance of $g_m/W \approx 1.5 \text{ mS}/\mu\text{m}$ (0.2 V bias). This value is comparable to that of the above nanotube device with $g_m/\pi d \approx 2 \text{ mS}/\mu\text{m}$.

These devices were later characterized according to the 8-scattering parameters up to 60 GHz. The transit frequency was measured at 15 GHz and the intrinsic frequency was estimated at 35 GHz. Unfortunately, these samples suffered from aging with a drop of transconductance by a factor 3. Therefore, we believe that a transit frequency of 100 GHz will soon be achieved.

1.4 Optimization of Nano-FETs as pulsed charge detector (Task 1.2, 1.5)

1.4.1 Impedance matching of NT-FETs

The initial plans to use a low capacitance post-amplifier for an active impedance matching scheme have been replaced by a passive 4:1 step-down transformer which is a noiseless process that restricts the measuring bandwidth (0.1–0.8 GHz). The cryogenic setup resolution has strongly benefited from the factor 4 improvement in the noise current resolution.

1.4.2 Modeling of NT-FETs

The ballistic 1-dimensional FET can be described using the scattering theory by taking a simple transmission distribution $D(E) = 1$ and $D(E) = 0$, respectively, above and below the barrier top $\Phi = \beta e V_g$. This corresponds to a ballistic classical barrier for which current and noise are thermally activated and determined by the high energy tail for $E \geq \Phi$ of the Fermi distribution $f_s(E)$, $f_d(E)$ in the source and drain leads. In this classical picture quantum partition noise in $D(1-D)$ is absent. Simple formulas are obtained for the conductance $g_d = \partial I / \partial V_d$, the transconductance $g_m = \partial I / \partial V_g$ and the noise conductance $g_n = S_I / 4k_B T_e$ for a 4-fold degenerate, single mode conductor:

$$g_d = \frac{4e^2}{h} f_d(\Phi)$$

$$g_m = \beta \frac{4e^2}{h} [f_s(\Phi) - f_d(\Phi)]$$

$$g_n = [f_s(\Phi) + f_d(\Phi)] = g_d + \frac{g_m}{2\beta}.$$

Our theory, which has two parameters, $f_s(\Phi)$ and $f_d(\Phi)$, and three measurable quantities, carries an internal consistency check as written above. The electronic temperature can be deduced independently from the $g_m(V_g)$ dependence.²

² J. Chaste *et al.*, submitted to Nano Lett.

The relation $g_n(g_d, g_m)$ as well as the $g_m(V_g)$ dependence have been verified experimentally at high frequency in NT-FETs (Figure 5) which qualify them as paradigm of 1-dimensional Nano-FETs. The analysis shows a hot electron distribution in the leads with $k_B T_e \sim 0.2eV_d$. in qualitative agreement with a thermal model based on the Wiedemann–Franz law.²

1.4.3 Shot-noise limited sensitivity of NT-FETs

From the noise measurement and the model we have been able to determined the best conditions for charge sensitivity ($V_g = 0.5V$, $V_d = -0.3V$, arrow in Figure 6) which correspond to $\delta q \leq 13 \cdot 10^{-6} e/Hz^{1/2}$.

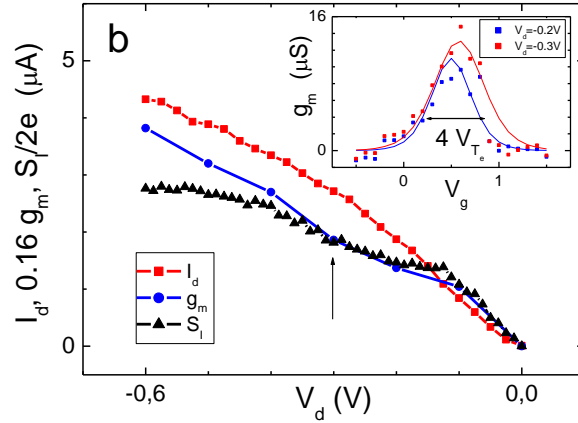
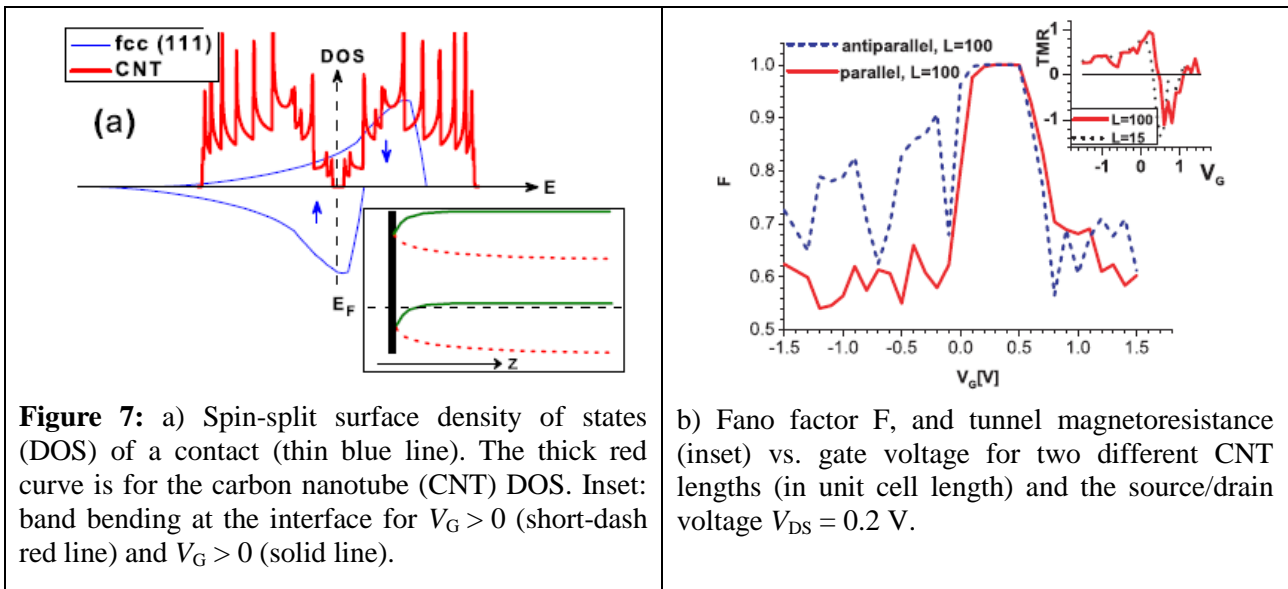


Figure 6: Active state with $V_g \sim +0.5$ V. RF noise $S_f(\omega)$ and transconductance g_m together with DC current I_d as a function of bias voltage V_d . (inset) RF transconductance $g_m(V_g)$ at $V_d = -0.2$ (resp. 0.3 V).

1.4.4 Theory of shot noise Schottky Barrier CNT-FETs

The Poznan node has studied the modeling of the SB CNT-FET operating at room temperature. The most important results of these studies concern determination of differential conductance, transconductance and shot noise (as well as the tunneling magnetoresistance, TMR, in the case of ferromagnetic contacts). It is noteworthy that TMR may reach quite large values up to several tens percent, while the shot noise in the off-state is mostly Poissonian and changes to the sub-Poissonian in the on-state. Figure 7a presents densities of states of both CNT (in red) and metallic electrodes (in blue), whereas the inset shows schematically the way the SB is formed. Figure 7b, in turn, shows the gate voltage dependence of the Fano factor (main panel) and the TMR (inset) for two different CNT lengths L (in units ~ 0.43 nm). The modeled transistor has a rather high TMR coefficient, and its signal-to-noise factor gets improved as the contacts are reoriented from the antiparallel configuration to the parallel one. These findings suggest that CNTs are very promising also for potential spintronic applications.



1.4.5 Single electron detection with NT-FETs

The direct demonstration of single electron sensitivity of NT-FETs has been done in the DC limit at ICN during the first period of the project. Experiment consisted in monitoring with single electron resolution the fluctuations and relaxation of the number of electron on a gold nano-particle weakly coupled by a tunnel barrier to the detecting semi-conducting nanotube (see Figure 8). The bandwidth was limited by the RC charging time of the particle in the hundreds of millisecond range, corresponding to attoampere charging currents.³

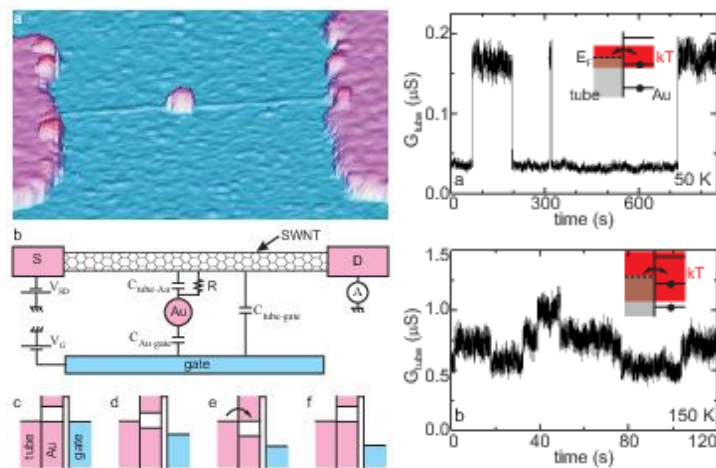


Figure 8: Demonstration of single electron detection scheme at the nanosecond time scale. A gold nano-particle is deposited on a semiconducting single wall carbon nanotube. Tunnel coupling allows for electron exchange between nanotube and particle. Single electron events can be resolved at the quasi-DC limit.

³ A. Gruneis, M. Esplandiù, D. Garcia-Sanchez and A. Bachtold, *Detecting Individual Electrons Using a Carbon Nanotube Field-Effect Transistor*, *Nano Lett.* **7**, 3766 (2007).

2 WP2 – Carbon nanotube rf-SET

2.1 Summary

The work of **WP2** has concentrated in understanding phenomena that affect charge sensitivity in rf-SET type of devices. We have investigated gate modulation both theoretically and experimentally, and obtained a quite good overall understanding of the phenomena. Charge detection sensitivity using SWNT rf-SETs has been brought to a new level: Our charge sensitivity of $\delta q = 2.3 \cdot 10^{-6} e/\text{Hz}^{1/2}$ at 4.2 K is seven times better than reached earlier in nanotubes, while our gain-bandwidth product of $3.7 \cdot 10^{13} \text{ Hz}^{3/2}/e$ is by more than one order of magnitude better than for typical radio-frequency single-electron transistors.

Our analysis on the non-equilibrium phenomena using shot noise thermometry have allowed us to determine the electron-phonon coupling both in the case of electron - acoustic phonon as well as electron - optical phonon scattering. These studies indicate that hot electron effects are important in our samples and that they limit the ultimate sensitivity reachable with rf-SETs using the present-day cooled pre-amplifiers. Including hot electron effects, the sensitivity of our rf-SETs are shot noise limited, thereby fulfilling the objectives. Moreover, we have investigated the potential of SWNT resonant tunneling transistors (RTT) which are not as sensitive to heating effects as rf-SETs. With nanotube RTTs we achieved a charge sensitivity of $\delta q = 5 \cdot 10^{-6} e/\text{Hz}^{1/2}$.

In graphene, similar non-equilibrium phenomena as in CNTs have been found, the main difference coming from the linearly bias-dependent number of transport modes. The current tends to saturate as the voltage across graphene is increased, but never reaches a complete saturation as in metallic nanotubes. Another difference, according to modeling based on the Boltzmann equation, is that impurity scattering plays a role in graphene and the current saturation is affected by the balance between impurity and optical-phonon scattering.

Theoretically, we have investigated gate modulation in Fabry-Pérot, Kondo, and Coulomb blockade regimes. Conductance and shot noise have been calculated in many configurations relevant to the analysis of experimental data. Special attention has been put to non-equilibrium states generated by AC fields. As compared with the regular Fabry-Pérot pattern, the AC modulation leads to a strong modification of the interference intensity, and can even lead to a phase inversion of the pattern. These phenomena might serve as a novel basis of THz detection with CNTs.

In our non-equilibrium studies, we have investigated thermal transport by phonons in CNTs and in graphene. Electronics applications require not only high electrical transmission but also large values for thermal conductance in order to allow for dense packing of devices. Thermal transport is strongly influenced by the dimensionality of a nano-scale system and we have addressed the additional modifications in phonon transport due to disorder. We find that isotopic disorder, or more generally Anderson-like disorder in force constants, leads to energy-dependent modification of the lattice thermal conductance in CNTs. In GNRs, we find a very strong reduction of phonon transmission due to edge disorder, while the Anderson-like disorder has less effect.

2.2 Gate modulation (Task 2.2)

Gate modulation has been measured on a multitude of samples paying special attention to combined effects: superconductivity and Coulomb blockade, multiple Andreev reflection and Coulomb blockade, quantum dot formation due to screening and Schottky barriers, etc. At the same time we have been looking for ways to utilize these combined phenomena. Gate modulation forms the cornerstone on which the device action of this work package is based on. These issues have already been addressed in WP1 in the case of semiconducting samples. In WP2, we have

been dealing with metallic devices in which the contact quality influences strongly the gate modulation pattern. Different characteristics are obtained for: 1) Fabry-Pérot regime, 2) Kondo regime, and 3) Coulomb blockade regime. We have investigated all of these regimes.

2.2.1 Fabry-Pérot regime and contact transparency

We have made detailed investigations, both experimentally and theoretically, on conductance and shot noise in the Fabry-Perot regime. Results of our theoretical calculations are illustrated in Figure 9. The differential conductance through a two-terminal setup of carbon nanotube of different lengths and chiralities was studied. The distance between the Fabry-Pérot oscillations in the gate voltage V_{gate} depends on the total gate capacitance, while in the bias voltage V_{bias} depends directly on the level spacing (i.e. on the length). The results in Figure 9 indicate clearly that chirality influences the modulation of the interference pattern: Zigzag tubes appear to yield more smooth sinusoidal variation than the armchair ones.

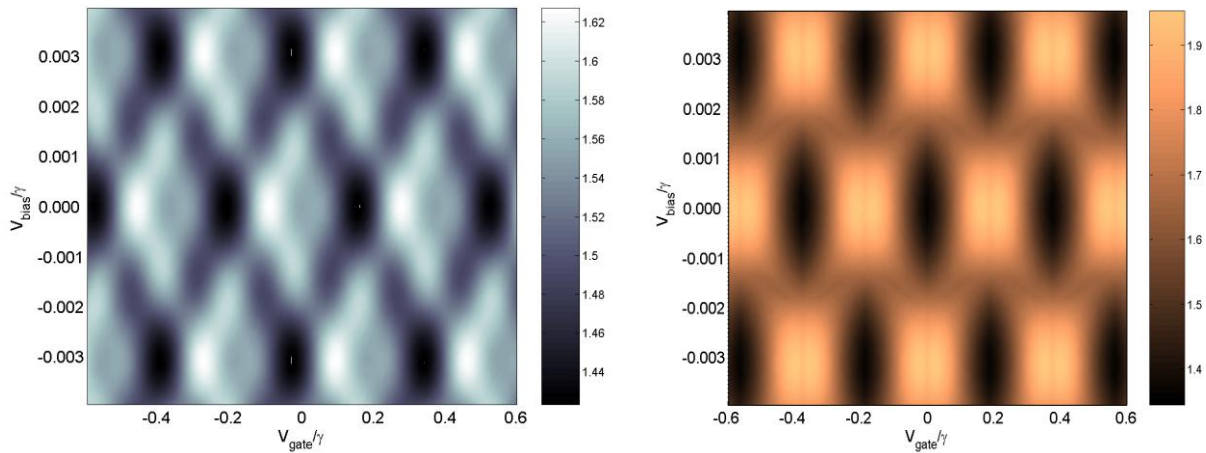


Figure 9: Differential conductance as function of the gate and bias voltages for an armchair nanotube (left) and a metallic zigzag carbon nanotube (right). The two tubes used here have similar lengths (a bit over 210 nm) to reflect the differences arising from the different chiralities. The number of atoms in the central region is then over 10000. One can observe the different shapes appearing: sharper diamonds for the armchair CNT and oscillations with a more sinusoidal shape for the zigzag CNT.

Conductance and shot noise experiments were performed in Helsinki and Paris in a complementary fashion. The Paris node concentrated on the small bias regime and shot noise at low frequencies⁴ while in Helsinki noise was measured at microwave frequencies up to high bias.⁵ The results of the Helsinki node on a 300 nm long SWNT sample with Ti/Al contacts are illustrated in Figure 10a for differential conductance and in Figure 10b for the differential shot noise. The patterns can be interpreted in terms of two transmission channels with average transmissions of $\tau_1 = 0.48$ and $\tau_2 = 0.13$. The modulation of the transmission is found to be on the order of 50 %. Alternatively, these FP-resonances can be modeled with non-interacting Breit-Wigner resonances. The Breit-Wigner model, on the other hand, can be employed to estimate critical currents for the SNS tunnel contacts (see WP4).

⁴ L.G. Herrmann, T. Delattre, P. Morfin, J.-M. Berroir, B. Plaçais, D.C. Glattli, and T. Kontos Phys. Rev. Lett. **99**, 156804 (2007).

⁵ F. Wu, P. Queipo, A. Nasibulin, T. Tsuneta, T. H. Wang, E. Kauppinen, and P. J. Hakonen, *Shot Noise with Interaction Effects in Single Walled Carbon Nanotubes*, Phys. Rev. Lett. **99**, 156803 (2007).

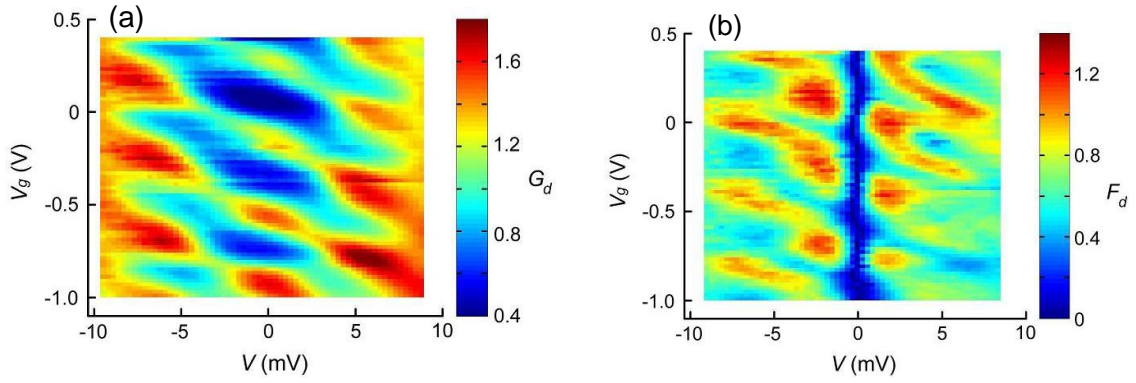


Figure 10: (a) Differential conductance on the bias vs. gate voltage plane for a SWNT sample. The conductance scale on the right is given in terms of G/G_0 , where $G_0 = e^2/h$ corresponds to the conductance of one quantum channel. (b) Differential Fano factor defined by $F_d = 1/(2e) dS/dI$. Total F and G are obtained from these results by integration along the bias axis.

2.2.2 Kondo regime

Kondo regime has been investigated thoroughly in CARDEQ in the context of proximity induced superconductivity in single walled nanotubes. Even π -junctions could be produced owing to the competition of Kondo effect and Josephson coupling (see WP4). We have also found that the bias dependence of the Kondo resonance influences the proximity-induced supercurrent of an individual SWNT:⁶ resonances with zero-field splitting result in a smaller critical current than for the regular Kondo maxima. These resonances are indicated in Figure 11 which displays a differential conductance scan on the plane spanned by bias voltage V_{ds} and gate voltage V_g measured at $B = 70$ mT.

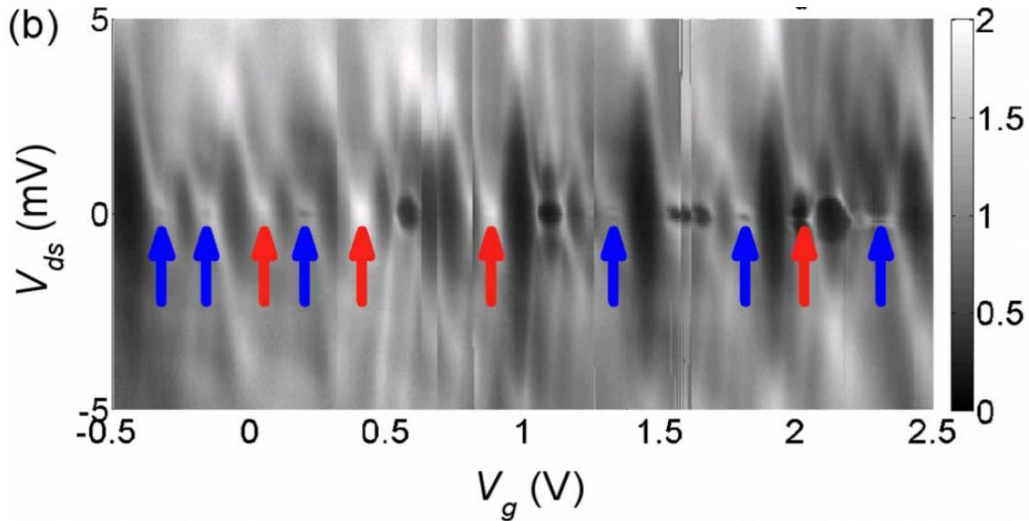


Figure 11: Normal state differential conductance G_d (in units of e^2/h) on the plane spanned by bias voltage V_{ds} and gate voltage V_g in Kondo regime at $T = 30$ mK. Normal states were achieved with a magnetic field of $B = 70$ mT. Red and blue arrows in refer to two types of resonance peaks, which have one magnitude difference in critical current I_{CM} with similar Kondo temperature T_K . See Ref. 6 for more details.

Zero-field splitting seems to take place in our data in every second Kondo resonance, as seen in the nearly alternating sequence of red and blue arrows in Figure 11. Previously zero-field Kondo-peak splitting has been reported in Ref. 7, where the splitting originates from magnetic impurities, which is different from our case as the splitting should then be seen at all the Kondo

⁶ F. Wu, R. Danneau, P. Queipo, E. Kauppinen, T. Tsuneta and P. J. Hakonen, *Single-walled carbon nanotube weak links in Kondo regime with zero-field splitting*, Phys. Rev. B **79**, 073404 (2009).

⁷ J. Nygård, W. F. Koehl, N. Mason, L. DiCarlo and C. M. Marcus, arXiv:cond-mat/0410467 (unpublished).

resonances. Moreover, using the standard fourfold shell-filling sequence, it is hard to explain our findings. From the normal-state bias maps, the characteristic zero-field splitting energy can be estimated as the width of the zero-bias anomaly ~ 0.4 meV, which is well above the typical singlet-triplet excitation energy. We conjecture that the observed zero-field splitting is related to the SU(4) Kondo effect which is peculiar to carbon nanotubes and which has been shown to lead to a dip in the density of states at small energies.⁸ SU(4) Kondo can also explain the unusually high T_K by the enhanced degeneracy of a multiple-level quantum dot. More experimental work is still needed to pinpoint definitely the origin of these phenomena.

2.2.3 Coulomb blockade regime

Coulomb blockade regime is the most intensively studied regime in carbon nanotubes as all the samples with bad contacts fall into this category. The only aspect, in which CARDEQ work has contributed in this area, is in providing more evidence that the boundary between Fabry-Pérot and Coulomb blockade regimes is not so clear cut. There appears to be samples which are in the Fabry-Pérot regime even though the conductance of them is not very large (See Deliverable D14, Appendix II). This finding is in line with the earlier findings of H. Park and co-workers.⁹

2.3 Sensitivity of carbon nanotube radio-frequency electrometers (Task 2.4)

2.3.1 Radio-frequency single-electron transistor

Development of rf-SETs from nanotubes requires, on one hand, low transparency contacts for clear Coulomb modulation and, on the other hand, high transparency contacts for impedance matching. We have employed samples in the range 10–100 k Ω in our experiments. Our experimental methodology in the rf-SET measurements can be found in Deliverable D3. Experiments were performed over carrier frequencies 700–1600 MHz at 4.2 K and at 50–100 mK with rather similar outcome. Altogether we scanned about ten samples out of which three were suspended. For substrates, we used either SiO₂/Si or sapphire. The best results (see Ref. 10 for details), displayed in Figure 12, were obtained on tubes grown using CVD on sapphire as described in Deliverable D14.

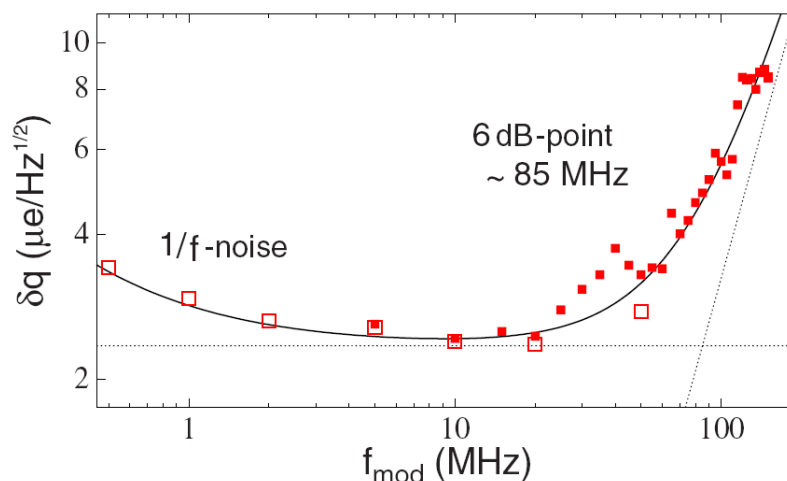


Figure 12: Charge sensitivity versus modulation frequency, with/without a 100 MHz low-pass filter on the gate line (open/closed symbols). The lines indicate the roll-off limited by the bandwidth and 1/f-noise at low frequency.

⁸ J. S. Lim, M.-S. Choi, M. Y. Choi, R. López and R. Aguado, Phys. Rev. B **74**, 205119 (2006).

⁹ W. Liang, M. Bockrath and H. Park, Ann. Rev. Phys. Chem. **56**, 475 (2005).

¹⁰ S. E. S. Andresen, F. Wu, R. Danneau, D. Gunnarsson and P. J. Hakonen, J. Appl. Phys. **104**, 033715 (2008).

The optimum rf-SET operating point was found by searching for conditions of perfect matching, i.e., vanishing reflection at the resonance frequency. The signal was homodyne detected by mixer, and the phase was tuned to be sensitive only to the real part of the SET impedance. Using a spectrum analyzer, the input carrier power was tuned to obtain a maximum signal-to-noise ratio of the sidebands at $f_0 \pm f_{\text{mod}}$, while keeping a small gate-charge modulation at a frequency $f_{\text{mod}} = 10$ MHz. The signal-to-noise ratio (SNR) of both sidebands yields a charge sensitivity of $2.3 \cdot 10^{-6} e/\text{Hz}^{1/2}$. Compared with previous carbon nanotube RF-SETs,¹¹ the enhancement is by about a factor of 7. The frequency response was mapped out by measuring the charge sensitivity over a range of modulation frequencies of 0.5–150 MHz (Figure 12). We found a bandwidth of 85 MHz using a 6 dB roll-off as the limit. For the use as a single charge detector, the nominal band width amounts to 300 MHz. Low-frequency $1/f$ -noise only contributes significantly below 1–2 MHz in this measurement.

As argued in Deliverable D14, the obtained sensitivity of $2.3 \cdot 10^{-6} e/\text{Hz}^{1/2}$ corresponds to the shot noise limited sensitivity when the heating effects due to carrier bias are taken into account.¹² There is no easy way out from this problem. It would require either preamplifiers of lower noise temperature (which do not exist at present) or better quality samples where the heating would go to the reservoirs only (and which themselves do not heat up). Owing to the heating, unfortunately, lowering the base temperature will not improve the situation.

2.3.2 Radio-frequency resonant tunneling transistor

In order to minimize hot electron effects, we have investigated an alternative option, a resonant tunneling transistors (RTT) made out of nanotubes in the Fabry-Pérot regime. The sensitivity of a nanotube RTT depends on the phase coherence length which varies slower with temperature than Coulomb effects. Therefore, it provides a vibrational detector less sensitive to hot electron effects than the rf-SET based detectors.

The differential conductance dI/dV_{ds} of our Fabry-Pérot device (see Deliverable D14) varies between 0.6 and $1.4 e^2/h$ ($= G_0$). Even though G is quite small, the absence of blockade regions indicates that our quantum dot is not in the Coulomb blockade regime. In addition to the zero-bias pattern, there are also conductance modulations around $V_{\text{sd}} = \pm 5$ mV identifying the Fabry-Pérot nature of the interference pattern. Similar low conductance Fabry-Pérot behavior has been reported for example in Ref. 9. The interference pattern, governed by the phase shift formula $\pm[eVl_{\text{tube}}/(\hbar v_{\text{F}}) + \pi l_{\text{tube}}C_L V_{\text{g}}/(4e)]$, corresponds well to the level spacing estimated for our sample with $l_{\text{tube}} = 0.3 \mu\text{m}$ and to the gate capacitance $C_{\text{g}} = l_{\text{tube}}C_L = 6.4$ aF obtained from the gate period of 70 mV. Unfortunately, the measured sensitivity, displayed in Figure 13, is not sufficient to make this device a good choice, as the equivalent charge sensitivity of our best RTT is by a factor of 2.5 worse than the sensitivity of the rf-SET described above (with hot electron effects). A full account of the RTT work is given in Appendix II of deliverable D14.

¹¹ L. Roschier, M. Sillanpää, W. Taihong, M. Ahlskog, S. Iijima and P. Hakonen, *J. Low Temp. Phys.* **136**, 465 (2004).

¹² See also: A. N. Korotkov and M. A. Paalanen, *Appl. Phys. Lett.* **74**, 4052 (1999).

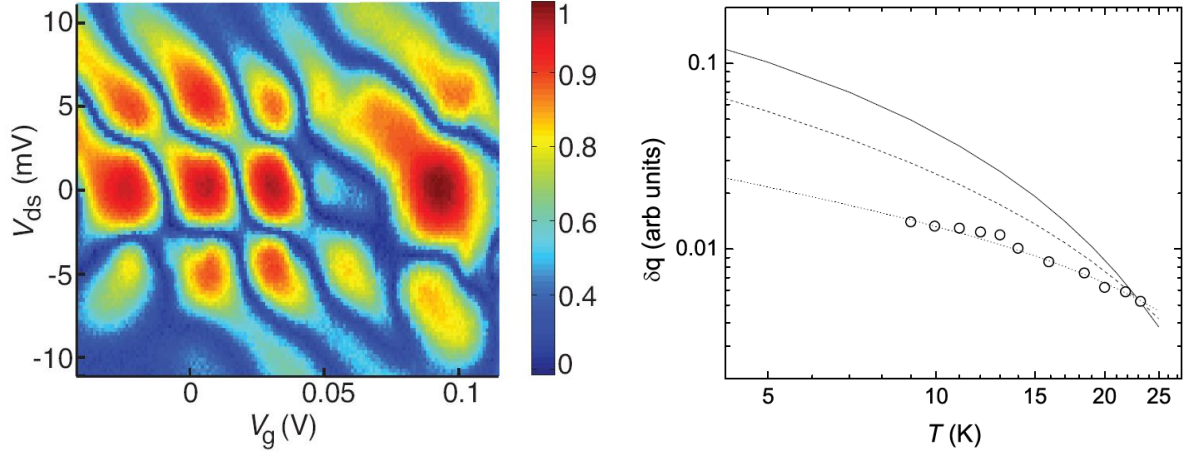


Figure 13: Left: 2D-map of the charge sensitivity as a function of gate voltage V_g and bias voltage V_{ds} . Colour bar on the right denotes $\delta q_{opt}/\delta q$, the inverse charge sensitivity $1/\delta q$ scaled with the inverse optimum sensitivity of $(\delta q_{opt})^{-1} = (5 \cdot 10^{-6} e/\text{Hz}^{1/2})^{-1}$. The gate period of this pattern is half of that of the period of the conductance pattern, which indicates that device is sensitive both at positive and negative slopes of $G(V_g)$ curve. Right: Charge sensitivity as a function of temperature. The solid curve is a model calculation for a double barrier resonant tunneling transistor using dephasing length $l_\varphi \propto T^\beta$ with $\beta = 1$ (solid), $\beta = 2/3$ (dashed), and $\beta = 1/3$ (dotted).

2.4 Electron-phonon coupling in nanotubes and graphene (Task 2.3)

2.4.1 Electron-phonon coupling in nanotubes

Theoretical calculations based on mean-free path type of arguments have been successful in explaining the observed IV characteristics of SWNTs, and they indicate hot-phonon generation with large phonon temperatures at large bias voltages.¹³ In addition, the energy relaxation between electrons and phonons has been probed by time-resolved photoelectron spectroscopy.¹⁴ Recently, high-bias electron-transport studies in conjunction with Raman spectroscopy have been performed and direct confirmation of the hot phonon temperatures of several hundred kelvins has been obtained.^{15,16} These investigations have addressed only the phonon temperature and the electronic temperature has not been determined. We have studied shot noise in single walled nanotubes at high bias and we have employed shot noise thermometry to determine the electronic temperature. We find good agreement with the reported optical phonon temperatures. Using this shot noise thermometry, we are also able to map out the electron phonon coupling for a single metallic nanotube as a function of temperature.¹⁷

For large electron-phonon or electron-electron scattering rates, the solutions of the diffusive Boltzmann equation tend towards a Fermi function, i.e., to a local equilibrium: $f(\varepsilon, x) \approx f_0(\varepsilon, V(x), T(x)) \equiv (\exp[(\varepsilon - V(x))/T(x)] + 1)^{-1}$, characterized by a local potential $V(x)$ and a temperature $T(x)$. Considering a 1-dim wire this yields:

$$F \equiv \frac{S}{I} = \frac{2}{LeV} \int_0^L dx \int_{-\infty}^{\infty} d\varepsilon f(\varepsilon, x)[1 - f(\varepsilon, x)] = \frac{2k_B}{LeV} \int_0^L dx T(x) = \frac{2k_B T_e}{eV}, \quad (1)$$

where T_e is the average electronic temperature. If thermal conduction is dominated by electronic conduction, the Poisson equation yields $T_e = \sqrt{3}/8 V$ and $F = \sqrt{3}/4$ which is the well-known

¹³ See, *e.g.*, E. Pop, D. Mann, J. Cao, Q. Wang, K. Goodson and H. Dai, Phys. Rev. Lett. **95**, 155505 (2005).

¹⁴ G. Moos, R. Fasel and T. Hertel, J. Nanosci. Nanotech. **3**, 145 (2003).

¹⁵ A. W. Bushmaker, V. V. Deshpande, M. W. Bockrath and S. B. Cronin, Nano Lett. **7**, 3618 (2007).

¹⁶ M. Oron-Carl and R. Krupke, Phys. Rev. Lett. **100**, 127401 (2008).

¹⁷ F. Wu, J.K. Viljas, P. Virtanen, S. Andresen, T. Heikkilä, B. Plačajs and P.J. Hakonen, to be published (2009).

theoretical estimate due to hot electrons at an internal equilibrium. Hence, there is a well defined connection between electronic temperature and Fano-factor, and we may employ this relation for thermometry in our nanotube samples.

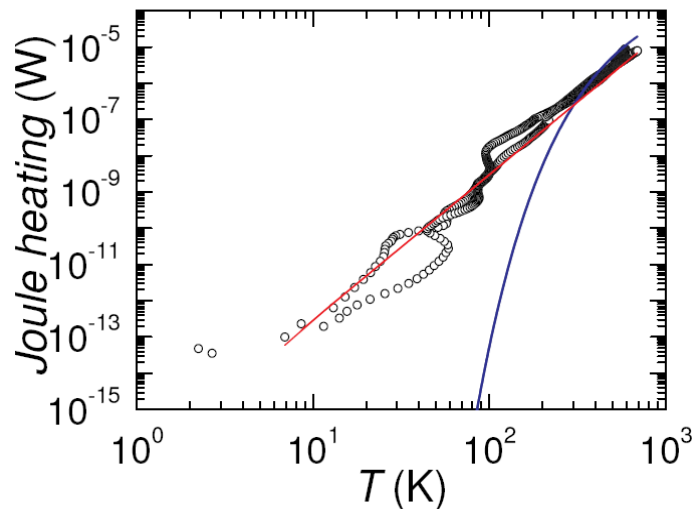


Figure 14: Electronic temperature T_e vs. Joule heating by bias voltage V_{ds} . Theory curves for acoustic phonons and for optical phonons are illustrated by the red and blue solid curves, respectively.

Figure 14 displays T_e deduced from F in terms dissipated power $P = V_{ds}^2/R$. A fit using $T_e^4 - T_0^4$ works best over the whole range of data, and this agrees with the calculation for electron-acoustic phonon heat transfer using zone-folding continuum approximation in SWNTs. The fitted red curve (in the intermediate bias range $20 \text{ mV} < V_{ds} < 200 \text{ mV}$, i.e. $100 \text{ K} < T_e < 350 \text{ K}$) yields $P = \Sigma(T_e^4 - T_0^4)$ where $\Sigma = 10^{-11} \text{ W}/(\text{m}\cdot\text{K}^4)$. The numerical value is somewhat larger than predicted theoretically, which may indicate enhancement of electron-phonon coupling due to disorder or by the presence of substrate.¹⁸ At $V_{ds} \lesssim 0.2 \text{ V}$ ($T_e \lesssim 350 \text{ K}$), optical phonons take over and we obtain a good fit using regular relaxation parameters for the optical phonon scattering¹⁹ and $\hbar\Omega = 0.2 \text{ eV}$. Our result displays a different power law compared with the work of Moos *et al.*,¹⁴ who obtain a power of $T_e^5 - T_0^5$ for a nanotube bundle. Our low-bias dependence $P \propto T^4$ is also different from the result $P \propto T^3$ of Appenzeller *et al.* who report $1/T_e$ for the electron-phonon scattering time.²⁰

2.4.2 Electron-phonon coupling in graphene

At large voltage bias, ballistic transport in graphene is expected to break down due to emission of optical (or zone boundary) phonons (OP), as has been observed in single-walled carbon nanotubes (SWNT). In monolayer graphene, the high bias behavior has been investigated by Meric *et al.*²¹ who observed a tendency to current saturation due to OP emission. Electron-phonon (e-ph) scattering is detrimental for the speed and for the transconductance of graphene devices, whereas for the shot noise OP emission may contribute in a beneficial way by suppressing current fluctuations.

We have measured conductivity and shot noise in short bilayer graphene samples at high bias. As in our nanotube work, we also use the Fano factor as a thermometer to measure the

¹⁸ M. Steiner, M. Freitag, V. Perebeinos, J. C. Tsang, J. P. Small, M. Kinoshita, D. Yuan, J. Liu and P. Avouris, *Nature Nanotech.* **4**, 320 (2009).

¹⁹ M. Lazzeri and F. Mauri, *Phys. Rev. B* **73**, 165419 (2006).

²⁰ J. Appenzeller, R. Martel, P. Avouris, H. Stahl and B. Lengeler, *Appl. Phys. Lett.* **78**, 3313 (2001).

²¹ I. Meric *et al.*, *Nature Nanotech.* **3**, 654 (2008).

electronic temperature. We find that at large bias voltages the shot noise is, indeed, suppressed due to phonon emission. We also observe that below the threshold for phonon emission, the current-voltage characteristics are nonlinear. Such behavior arises for ballistic graphene as a result of the energy-dependence of the number of transport modes. As a function of bias, we find a linear increase of σ which is levelled off above $V_{ds} \sim 0.2$ V. In the linear region a scaling law is found between the bias and gate voltage dependences of σ , which agrees with the theory for bilayers.^{22,23} Excess noise Fano factor F is found to first increase with bias and then to reach a maximum at $V_{ds} \sim 0.1$ V, above which F decreases. A mean-free-path type model is used to analyze the results. We assign the saturation of σ and the decrease of F to the creation of optical/zone boundary phonons. The agreement between the measured results and our model is good, as seen in Figure 15. (see also Ref. 24), and we conclude that both the electrons and the active OPs heat up to 1000 K in our measurements.

In single layer graphene, situation is more complicated as we have shown in Ref. 25.

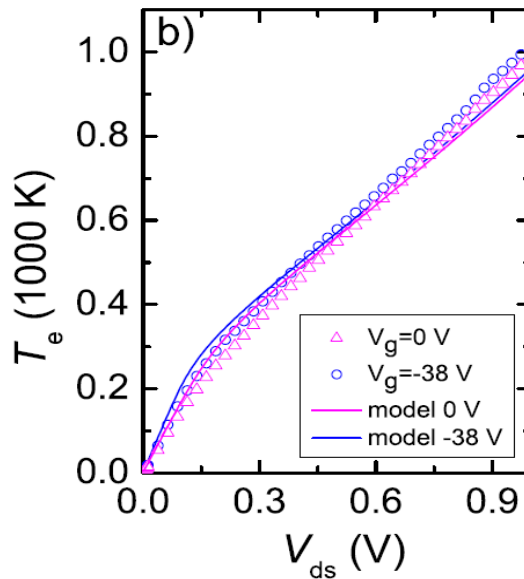


Figure 15: Electron temperature T_e as deduced from measured using shot noise thermometry at CNP (circles) and at $V_g = V_{g,CNP} + 38$ V (triangles); solid curves denote $T_e \approx T_{op}$ from our model with the same parameters given in Ref. 24.

3 WP3 – Control of the contact resistance

3.1 Summary

The work of WP3 has concentrated on contacting single walled and multiwalled carbon nanotubes, including some work on single layers of graphene. We have employed different metals for making the contacts as well as various cleaning/annealing procedures for improving their conductance. Ti and Pd have been found to be the most reliable metals for making the contacts. Gold, with a thin (2-3 nm) Ti or Cr sticking layer, is also quite good, and thanks to its stability, it has been used for etched, suspended samples .

²² I. Snyman and C.W.J. Beenakker, Phys. Rev. B **75**, 045322 (2007).

²³ A. H. Castro Neto *et al.*, Rev. Mod. Phys. **81**, 109 (2009).

²⁴ A. Fay, J. K. Viljas, R. Danneau, F. Wu, M. Y. Tomi, J. Wengler, M. Wiesner and P. J. Hakonen, arXiv:0904.4446 (2009).

²⁵ A. Barreiro, M. Lazzeri, J. Moser, F. Mauri and A. Bachtold, Phys. Rev. Lett. **103**, 076601 (2009).

The objectives have been successfully implemented to the extent that all experimental partners have demonstrated Pd- or Ti-based contacts to multi- or single-walled CNTs with conductance close to $4e^2/h = 4G_0$. The reproducibility, though, is within $\sim 30\%$ only with Pd contacts on MWCNTs that have $G = 3G_0$. Ti contacts mostly produce conductance below $2e^2/h$ but occasionally yield close to $4G_0$.

The development of superconducting contacts to single and multiwalled carbon nanotubes have been based on sandwich structures: Ti/Al/Ti, Ti/Nb/Ti and Pd/Nb/Pd. High transparency contacts have been obtained both to single and multiwalled tubes and the largest supercurrents have reached up to 4.8 nA and 30 nA, respectively. In single walled tubes, the contact transparency has varied from the Fabry-Perot regime via Kondo resonances to the fully Coulomb blockaded regime. Each of these regimes presents unique phenomena which we have addressed both experimentally and theoretically. In graphene, we obtained highly transparent contacts with Ti/Al, which gave a supercurrent on the order of 100 nA at the Dirac point.

The role of chirality on the contact resistance has been investigated theoretically in CNTs and, especially, in graphene. The studies have been based on either a semi-empirical approaches or *ab initio* electronic structure calculations. Mapping onto a tight-binding Hamiltonian has been employed in order to perform large scale transport calculations.

During the course of the CARDEQ program, strong effort was put in trying to make hybrid electronic structures out of CNTs and GaAs, i.e. to embed CNTs in to GaAs structures. Due to problematic issues with GaAs overgrowth, it was difficult to achieve proper contact between CNTs and a 2-dim electron gas in a GaAs quantum well. Instead, we have incorporated SWCNTs in to SiGe quantum wells, overgrown on SOI structures, and achieved resistances down to 140 k Ω .

3.2 Normal metal contacts (Task 3.3)

We have developed measuring methods where contact resistance is recorded after passing maximum current through the SWCNT. This means that the maximum possible in-situ annealing has taken place before the actual measurement is performed.

These studies are done using a scheme where we record the current–voltage characteristics while sweeping the bias until we observe that a nanotube burns away. By subtracting the zero-bias conductance values before and after, we deduce the value for the CNT that burned. This scheme has allowed us to collect statistics on the resistance values for individual CNTs from samples that contained several CNTs contacted in parallel.

The contacting materials used are Ti, Ti/Au, Pd, Pd/Au, Cr, and Cr/Au. In samples contacted with Pd we find a broad range of resistances $0-4e^2/h$. For Ti there is a tendency of values below $2e^2/h$ but they are more likely to archive higher values, when cooled to liquid helium temperatures. Cr and Cr/Au contacted CNT shows resistances in the $0-1e^2/h$ range are therefore most suitable for highly-resistive tunnelling contacts.

The Pd/Au sandwiched contacts were studied more detailed, to elucidate on the role of the Ti or Pd layer that is often used to create good contacts between CNT and a superconducting material Al or Nb, but using Au instead of these materials for a faster sample fabrication. We studied Pd contacts with thickness 4, 8 and 10 nm.

The most successful high transparency contacts that we have produced so far have been based on 10 nm Pd and 40 nm Au. These samples often yield conductance values of the order $2e^2/h$. Low temperature transport measurements illustrates that our CNTs are of excellent

quality, and they have allowed us to deduce further details on the contacts, especially to semiconducting CNTs.²⁶

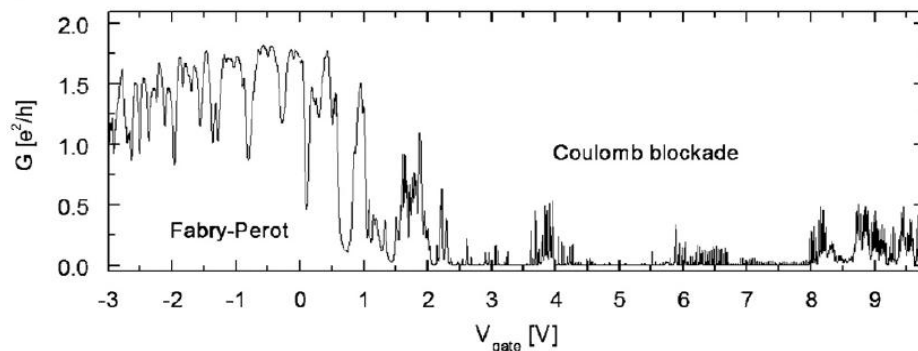


Figure 16: Low-temperature transport measurements at 4.2 K on a semiconducting SW-CNT contacted by Pd/Au (10/40 nm). The hole transport at negative gate voltage shows clear Fabry-Pérot interference, while the electron transport at positive gate voltage exhibits Coulomb blockade.

The low-temperature gate characteristics show the signature of a semiconducting CNT (Figure 16). It indicates that the palladium contacts are much more transparent to holes than to electrons. For negative gate voltages (p-type), we observe a clear Fabry-Pérot pattern as a signature of quantum interference. The conductance is then $1-2 e^2/h$. At positive gate voltage (n-type), the transport is dominated by quantum mechanical tunnelling, seen as Coulomb blockade diamonds with a clear level spacing. Here the conductance is only a fraction of e^2/h .

The difference in hole and electron transport is due to the different Schottky barriers that form between the SWCNT conduction/valence bands and the Fermi level of Pd. With the Fermi level pinned close to the valence band, a much shallower Schottky barrier is formed in the case of p-type gating than for n-type gating. That is also why the hole transport is already turned on at $V_{\text{gate}} = 0$ V.

Control over the Schottky barriers when contacting semiconducting carbon nanotubes is an important aspect of WP3. With palladium we have an ideal contact material for producing nearly perfect p-type contacts to semiconducting SWCNTs. In parallel, we would like to have a suitable material for n-type contacts. Therefore, we have started to implement scandium for contacting our single-walled carbon nanotubes.

Based on the combination of scandium and palladium for n- and p-type contacts, we have been able to construct a new and novel carbon nanotube device type. By contacting semiconducting SW-CNTs by Pd and Sc in each end, the different polarities lead to a depletion quite similar to that of a PIN diode. The current-voltage characteristics show rectifying diode behaviour with additional photocurrent induced by optical illumination (Figure 17).

²⁶ K. Grove-Rasmussen, H. I. Jørgensen and P. E. Lindelof, *Fabry-Pérot interference, Kondo effect and Coulomb blockade in carbon nanotubes*, *Physica E* **40**, 92 (2007).

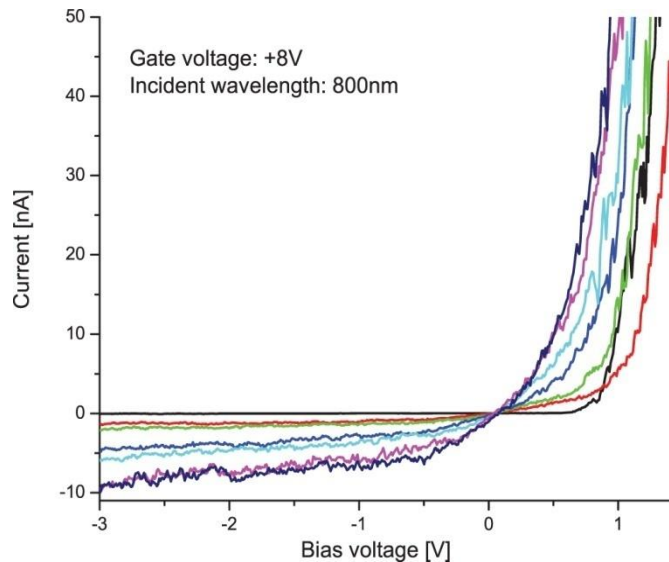


Figure 17: Current–voltage characteristics of a semiconducting SWCNT sample, contacted by Sc versus Pd in each end. Coloured curves correspond to increasing light illumination.

3.3 Superconducting contacts (Task 3.4)

3.3.1 Single walled carbon nanotubes (SWCNT):

We have worked with different contacting materials for superconducting contacts. For SWCNT the following material combinations have been used Ti/Al/Ti, Ti/Nb/Ti and Pd/Nb/Pd. The thin layer of Pd or Ti is sandwiched in the interface to get a better contact to the CNT while the top layer is to avoid oxidation. The different devices fall into three categories: Fabry-Pérot^{27,28} ($R < h/2e^2$), Kondo^{29,30} ($h/2e^2 < R < h/e^2$) and Coulomb blockade^{30,31} ($R \gg h/e^2$), where R is the contact resistance. We have produced and measured SWCNT in all three categories. In some of the semiconducting samples the contact resistance is primarily due to Schottky barriers at the interface. The Schottky barriers can be varied by the gate voltage making it possible to tune the transport properties of the SWCNT device into any of the three regimes mentioned above (Figure 18). In all three regimes clear effects of the superconducting electrodes have been observed.

²⁷ H. I. Jørgensen, K. Grove-Rasmussen, K. Flensberg and P. E. Lindelof, *Critical and excess current through an open quantum dot: Temperature and magnetic-field dependence*, Phys. Rev. B **79**, 155441 (2009).

²⁸ H. I. Jørgensen, K. Grove-Rasmussen, T. Novotny, K. Flensberg and P. E. Lindelof, *Electron Transport in Single-Wall Carbon Nanotube Weak Links in the Fabry-Pérot Regime*, Phys. Rev. Lett. **96**, 207003 (2006).

²⁹ K. Grove-Rasmussen, H. I. Jørgensen and P. E. Lindelof, *Kondo resonance enhanced supercurrent in single wall carbon nanotube Josephson junction*, New J. Phys **9**, 124 (2007).

³⁰ H. I. Jørgensen, K. Grove-Rasmussen, T. Novotny, K. Flensberg and P. E. Lindelof, *Critical Current $0-\pi$ Transition in Designed Josephson Quantum Dot Junctions*, Nano. Lett. **7**, 2441 (2007).

³¹ K. Grove-Rasmussen, H. I. Jørgensen, B. M. Andersen, J. Paaske, T. S. Jespersen, J. Nygård, K. Flensberg and P. E. Lindelof, *Superconductivity-enhanced bias spectroscopy in carbon nanotube quantum dots*, Phys. Rev. B **79**, 134518 (2009).

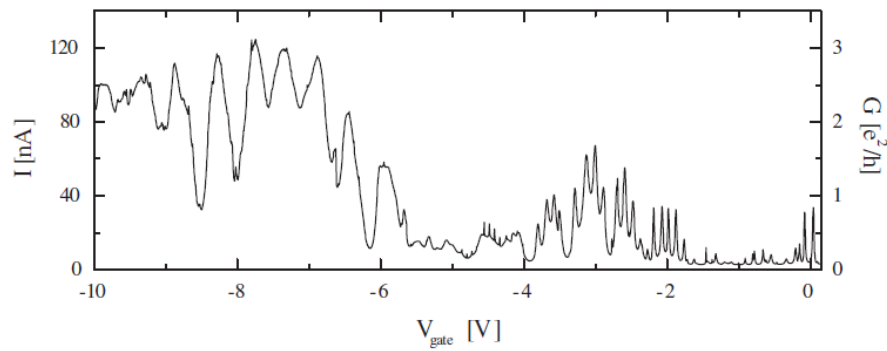


Figure 18: Current and conductance as a function of voltage applied to the back gate with 1 mV source-drain voltage, for a SWCNT device with superconducting contacts. The high conductance regime with Fabry-Pérot oscillations is reached at large negative gate voltages and Coulomb blockade is observed at lower gate voltages.

3.3.2 Multiwalled carbon nanotubes (MWCNT):

In MWCNT devices with Pd/Nb contacts were investigated³². The high quality of our junctions results from the excellent contact properties of the thin palladium interlayer and the expertise of patterning small niobium structures. The devices were found to be very reproducible and long-term stable. A pronounced overall variation of the contact transparency with gate voltage V_G was observed: for positive V_G the interface transparency was lower, resulting in well developed Coulomb diamonds and very small supercurrents. At negative V_G the contact transparency increases and pronounced supercurrent resonances appear. These resonances have a width that corresponds to the transfer of about 10 electrons and are thus considerably wider than the individual Coulomb resonances observed at positive V_G .

Diffusive MWCNT was also investigated using superconducting electrodes made of a Ti/Al/Ti sandwich. For more results of the superconducting devices see WP4 and D18.

3.3.3 Renormalization of orbitals in superconducting electrodes

When a single energy state is coupled to a continuum of states it will hybridize with the continuum leading to a renormalization of the single-states energy. It is often observed that the coupling to the two orbitals in a SWCNT is different. In the case of ferromagnetic contacts the coupling of the spin states can also differ. This difference in the coupling, leads to a different gate dependent renormalization of the orbitals or the spin states. We have observed such effects in SWCNT contacted with normal³³ (Figure 19), ferromagnetic³⁴ (Figure 20) and superconducting contacts³⁵ (Figure 21) where it gives rise to gate-dependence of the co-tunneling lines and shift of the Coulomb diamond edges.

³² E. Pallecchi, M. Gaaß, D. A. Ryndyk and Ch. Strunk, *Carbon nanotube Josephson junctions with Nb contacts*, Appl. Phys. Lett. **93**, 072501 (2008).

³³ J. V. Holm, H. I. Jørgensen, K. Grove-Rasmussen, J. Paaske, K. Flensberg and P. E. Lindelof, Phys. Rev. B **77**, 161406 (2008).

³⁴ J. R. Hauptmann, J. Paaske and P. E. Lindelof, Nature Phys. **4**, 373 (2008).

³⁵ K. Grove-Rasmussen, H. I. Jørgensen, B. M. Andersen, J. Paaske, T. S. Jespersen, J. Nygård, K. Flensberg and P. E. Lindelof, Phys. Rev. B **79**, 134518 (2009).

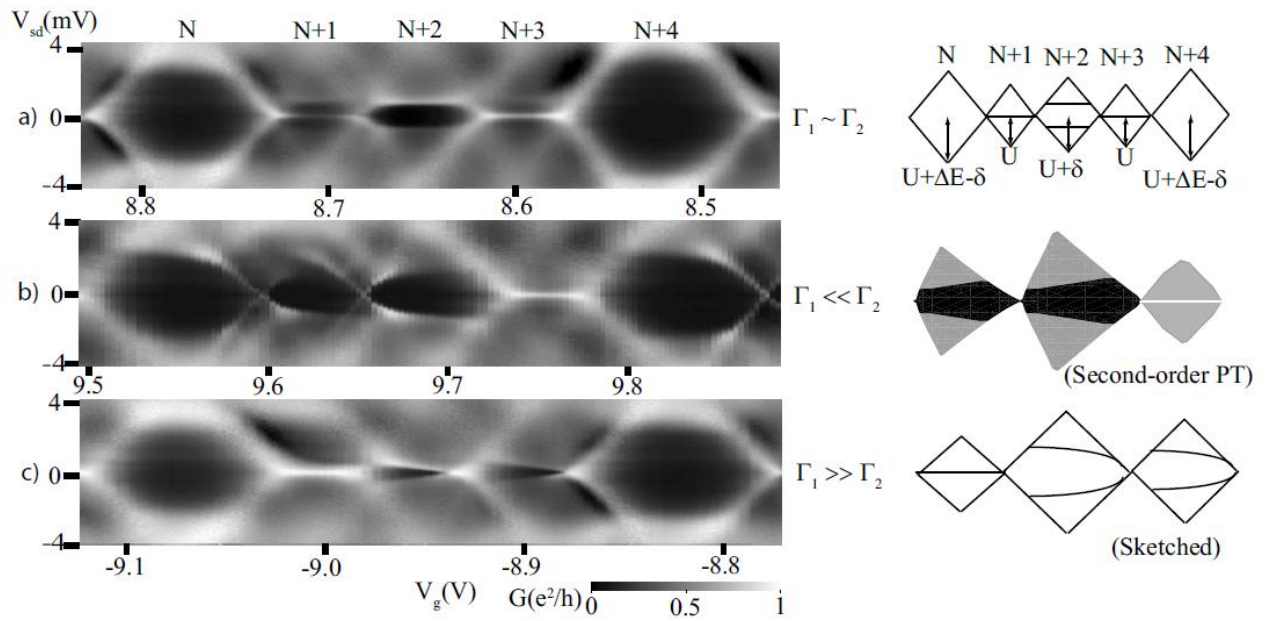


Figure 19: Differential conductance as a function of bias voltage (V_{sd}) and gate voltage (V_g) (left) on SWCNT with normal contacts. Schematic of the four-electron shells (right). (a) Four-electron shell filling for $\Gamma_1 \sim \Gamma_2$, with strong enough coupling to facilitate Kondo ridges in the $N+1$ and $N+3$ diamonds, as shown in the schematic. (b) Four-electron shell filling for $\Gamma_1 \ll \Gamma_2$. In the $N+1$ and $N+2$ diamonds, the inelastic cotunneling threshold has clearly acquired a gate dependence. Here, the right panel shows the cotunneling thresholds and diamond edges as calculated within second-order PT (the white Kondo ridge is drawn by hand). (c) Four-electron shell filling for $\Gamma_1 \gg \Gamma_2$. Gate-dependent cotunneling thresholds are now observed in the $N+2$ and $N+3$ diamonds instead. In the shell sequences where $\Gamma_1 \gg \Gamma_2$ or $\Gamma_1 \ll \Gamma_2$, the gate-dependent cotunneling threshold ridges inside the diamonds appear to form a U or V lying down with the openings facing the zero-bias Kondo ridge. Together the two U's (V's) and the Kondo ridge resemble a two-headed arrow, where the U (V) forms the two heads and the Kondo ridge the shaft. This means that the three center diamonds in the different domains have cotunneling and Kondo ridges, which can be schematically summarized as: $\Gamma_1 \sim \Gamma_2$: $- = -$; $\Gamma_1 \ll \Gamma_2$: $< < -$; and $\Gamma_1 \gg \Gamma_2$: $- > >$.

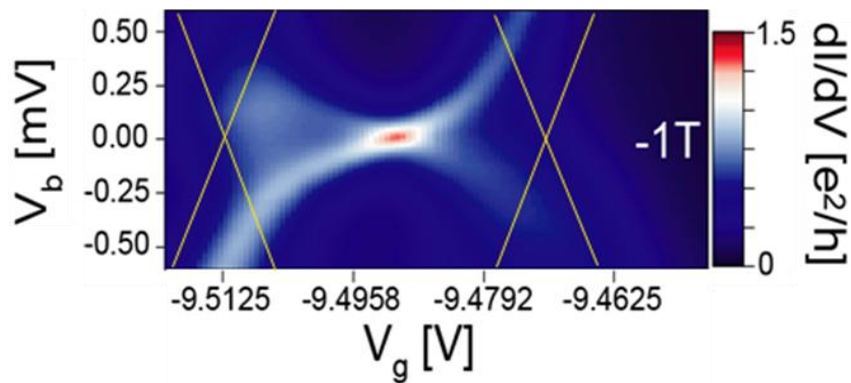


Figure 20: Differential conductance (dI/dV_{sd}) as a function of gate voltage (V_g) and bias voltage (V_{sd}) measured on a SWCNT with ferromagnetic contacts. The measurements is made in a magnetic field of 1T the yellow lines indicates the Coulomb diamond edges. The Kondo ridge seen in the measurements is degenerated in the middle of the Coulomb diamond, at the red point, and split as we tune the gate-voltage close to the Coulomb resonances. Measurements at higher magnetic fields show that spin up is the ground state to the left and spin down to the right.

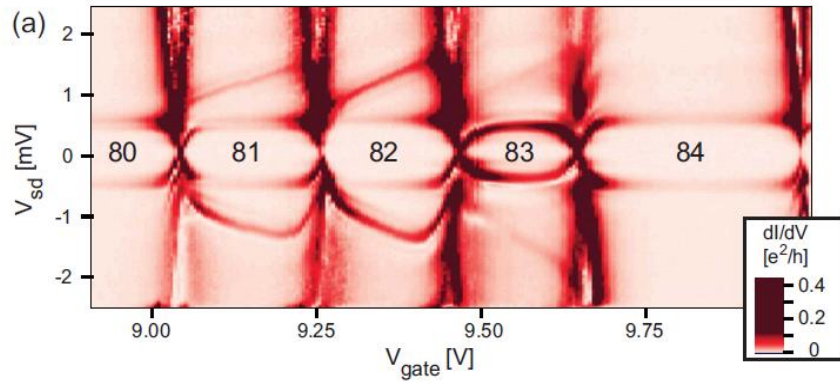


Figure 21: Differential conductance as a function of bias voltage (V_{sd}) and gate voltage (V_g) on a superconducting device with Pd/Nb/Pd contacts. Gate dependent cotunneling lines can be observed.

3.4 Cleaning by ion etching (Task 3.1)

We concluded on the basis of the results of the first year, that this cleaning scheme had to be abandoned as an unfruitful avenue and new approaches had to be sought for.

We have made investigations on contact resistance control using ion irradiation after the manufacture of the contact. Thus, instead of cleaning the nanotube and making the interface as ideal as possible, as originally planned in Task 3.1, we have tried ion-beam-induced local welding/amorphization/sputtering treatment which, if the contact material is properly chosen, will lead to substantial reduction of the contact resistance. In our first tests using Ti/Al on multiwalled carbon nanotubes, it has been possible to heal broken contacts by the ion irradiation treatment. The best two-lead resistance after ion irradiation was 13 k Ω . These findings suggest that non-local ion beam irradiation may provide a scalable way to overcome contact resistance as a hurdle for mass production of MWCNT based electronics.

3.5 Role of nanotube chirality (Task 3.2)

Initially, the idea was to try diffraction imaging on TEM to determine the chirality of SWCNTs. However, with the development of RAMAN techniques we have started to move towards optical techniques as they provide methods to investigate ready-made, contacted samples on bulk substrates. A Micro-Raman setup with a few distinct laser wavelengths will be sufficient to make a reliable identification of the characteristics of small single walled tubes. See the 2nd Activity Report for further details and problems in this approach.

The role of chirality on the contact resistance has been investigated theoretically in CNTs and, especially, in graphene. We have developed a semi-empirical approach able to model the electronic structure of the contact region composed of a graphene layer and the metal surface.³⁶ The *ab initio* electronic structure results were mapped onto a tight-binding Hamiltonian that was used to perform large scale transport calculations. Our efforts now focused on full non-equilibrium transport calculations in which a bias voltage is applied to real metallic contacts of Ti/Pd placed onto a graphene sheet. In Ref. 37, *ab initio* studies have been performed for realistic materials (Co, Ni and Cu) in contact with multilayer graphene. The metal contacts were put on both sides of graphene, and perpendicular transport in the presence of structural disorder was calculated. Optimum geometry of the interface was determined in terms of interface atom distances and their respective locations. It turns out that graphene acts as a spin filter in the case when contacts are ferromagnetic. The effect stems from the near perfect lattice match and the

³⁶ N. Nemeč *et al.*, Phys. Rev. Lett. **96**, 076802 (2006); N. Nemeč *et al.*, Phys. Rev. B **77**, 125420 (2008).

³⁷ V. M. Karpan, P. A. Khomyakov, A. A. Starikov, G. Giovannetti, M. Zwierzycki, M. Talanana, G. Brocks, J. van den Brink and P. J. Kelly, *Theoretical prediction of perfect spin filtering at interfaces between close-packed surfaces of Ni or Co and graphite or graphene*, Phys. Rev. B **78**, 195419 (2008).

relation between projected Fermi surfaces (FS) of the contacted materials. The lack of the overlap between projections for majority channel FS means that the only contribution to transmission comes from the minority channel provided that the number of graphene layers is sufficient to exclude the tunnelling contribution. The effect is remarkably robust and only moderately diminished in the presence of disorder. Additionally the effect of the small lattice mismatch between aforementioned metals and graphene was estimated by means of calculations utilizing lateral supercells of different sizes and found to be negligible.

3.6 Integration of carbon nanotubes into semiconducting structures (Task 3.5)

As outlined in detail by our deliverable report D10, we have attempted a number of different strategies for contacting SWCNTs by epitaxial overgrowth. Originally, this topic was targeted at incorporating SWCNTs into GaAs based heterostructures, though we have extended our work to include also silicon, most recently in the form of overgrown SOI structures. The SWCNTs are introduced prior to overgrown, either from liquid dispersion or by CVD growth directly on the silicon or SOI substrate.

Our progress on the GaAs overgrowth has been limited by severe problems with the epitaxy. When growing at more than 400 °C, needed for sufficient doping, the layers form deep trenches over the nanotube sites. Hence, it has proven impossible to produce electrical contacts to SWCNTs by GaAs overgrowth. Instead, we have instigated work on silicon based heterostructures and SOI. As outlined in the D10 report, there has been great progress on the SOI structures in particular. The contacts produced by overgrowth of heavily doped layers (both n- and p-type) yield resistances of $\sim 1\text{ M}\Omega$, and FET characteristics were obtained for semiconducting nanotubes.

Due to the issues with GaAs overgrowth, it has been difficult to meet the milestone “Contact from a SWCNT to a 2-dimensional electron gas in a GaAs quantum well”. We have studied the incorporating of SWCNTs in SiGe quantum wells, overgrown on SOI structures. The electrical measurements give resistances down to 140 k Ω .

3.7 Graphene

Since graphene was taken up later, the work on graphene contacts forms a small fraction of the amount that was performed on CNT contacts. The contact resistance between the biasing leads and graphene can strongly affect electrical transport and shot noise. This resistance has to be well known in order to extract results intrinsically related to the graphene flake alone. In general, small contact resistance is preferable and is looked for. We have employed Ti/Al and Pd/Nb contacts and found that both work very well at low temperatures. Primarily, these contacts are employed for obtaining proximity induced supercurrents (see Deliverable D27). We find that Pd/Nb contacts are better than Ti/Al contacts for this purpose: Ti/Al contacts present a resistance of $\sim 15\ \Omega$ while for a Pd/Nb contact the resistance is practically zero. However, at higher temperatures the Ti/Al contacts perform better (see 3rd yearly Activity Report).

4 WP4 – Superconducting nanotube transistor

4.1 Summary

WP 4 has established the development of CNT-based Josephson junctions as planned in the proposal. Concerning the gate control of the Josephson current in single- and multi-walled CNTs, substantial progress has been made in our experimental work, and several different regimes of nanotube Josephson junctions have been investigated.

In FP regime, critical currents up to 4.8 nA have been observed. In this regime, the nanotube together with superconducting leads can be considered as a resonant level quantum dot, and thus the two-barrier Breit-Wigner model is applicable to model its behavior. In our case, the measured I_C is nearly one order of magnitude smaller than the theoretical prediction $I_0 \sim 30$ nA with one resonant spin-degenerate level. However, by taking into account phase diffusion due to environmental noise, a reasonably good agreement can be obtained.

In the Kondo regime, novel π -junctions have been produced and analyzed in detail. The Kondo regime, in fact, is very rich in phenomena and a lot of additional work is needed before it becomes fully understood. The CARDEQ work has just scratched the surface so far. In multiwalled tubes, we have also reached good contact transparency, but scattering in the tube affects strongly the gate modulation pattern. Instead of a Fabry-Perot interference, the patterns are reminiscent of universal conductance fluctuations. The scattering also leads to diffusive proximity junctions in multiwalled tubes, contrary to the resonant junction of short single walled tubes.

Although the representative values of supercurrents have remained rather small, about 5 nA or less, it has been possible to employ these junctions successfully in the high-frequency regime. We have demonstrated that, using a superconducting nanotube sample with critical current of around 2.5 nA, it is possible to construct an rf-electrometer with a charge sensitivity (see D19) equal to $4 \cdot 10^{-5} e/\text{Hz}^{1/2}$ which is a typical value for a regular rf-SET. The operating band of this device, 600-900 MHz, is limited only by the performance of the circulators and of the preamplifier. In addition, we have demonstrated the applicability of the non-hysteretic rf-SQUID concept for nanotube Josephson junctions: i.e. we have employed a weakly capacitively coupled LC resonant circuit as an inductance-frequency converter for a nanotube junction mounted in parallel to the resonant circuit. In graphene junctions, we employed the same principle and measured their current-phase relation (CPR). Due to the strongly non-sinusoidal character of the CPR, the phase responsivity of these devices is excellent which suggests their use in phase detectors at the quantum limit.

We have approached the regime of “large” supercurrents by using Nb/Pd-bilayers as the contact material with a superconducting gap of $\Delta \sim 1$ meV. So far this has been successful with multiwalled tubes and, in the next generation of investigations, it will work, we believe, also with SWCNTs.

In addition, to two-terminal devices, three-terminal configurations containing one superconducting and two normal contacts have been studied. Such structures, called as “Cooper pair beam splitters” allow a spatial separation of potentially spin-entangled electron pairs, injected from the superconductor into a double quantum dot formed by the SWNT. We have done experiments on a Cooper pair beam splitter, and our data strongly support the presence of substantial crossed Andreev reflections, i.e. splitting of a significant fraction of the injected Cooper pairs. Our work is one of the first experimental realizations of a Cooper-pair beam splitter and opens new possibilities to investigate spin-entangled electrons and their application in quantum information processing.

4.2 Induced superconductivity in multi-walled CNTs (Task 4.1)

In Regensburg, MWCNT weak links between Nb/Pd-leads have been investigated. The high quality of the junctions results from the excellent contact properties of the thin palladium interlayer and our expertise of patterning small niobium structures. A pronounced overall variation of the contact transparency with gate voltage V_G was observed: for positive V_G the interface transparency was lower, resulting in well developed Coulomb diamonds and very small supercurrents (see Figure 22). At negative V_G the contact transparency increases and pronounced

supercurrent resonances appear. These resonances have a width that corresponds to the transfer of about 10 electrons and are thus considerably wider than the individual Coulomb resonances observed at positive V_G .

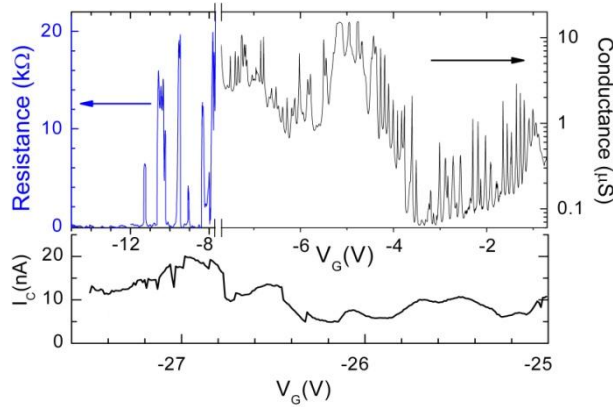


Figure 22: Top: Zero bias resistance (left part) and conductance (right part) of the sample vs. V_G at 25 mK. The height of the resistance maxima varies by 4 orders of magnitude in the V_G -range shown. Bottom: Critical current at more negative V_G . The supercurrent resonances merge, but remain still visible. At very negative V_G background charge switching events appear.

Figure 22 illustrates the I_C -characteristics of an individual supercurrent resonance with an intermediate height of ~ 8 nA. This value is already twice larger than reported for Al-based CNT-junctions and very stable in time. At more negative V_G even $I_C \sim 30$ nA was observed, but in this regime instabilities most probably induced by back-ground charge switching are more frequent. The IV -curves are hysteretic at most temperatures and gate voltages and the recorded switching histograms (see Figure 23a) are very narrow. This demonstrates a proper design of the electromagnetic environment of our junctions, which minimizes premature switching induced by phase fluctuations.

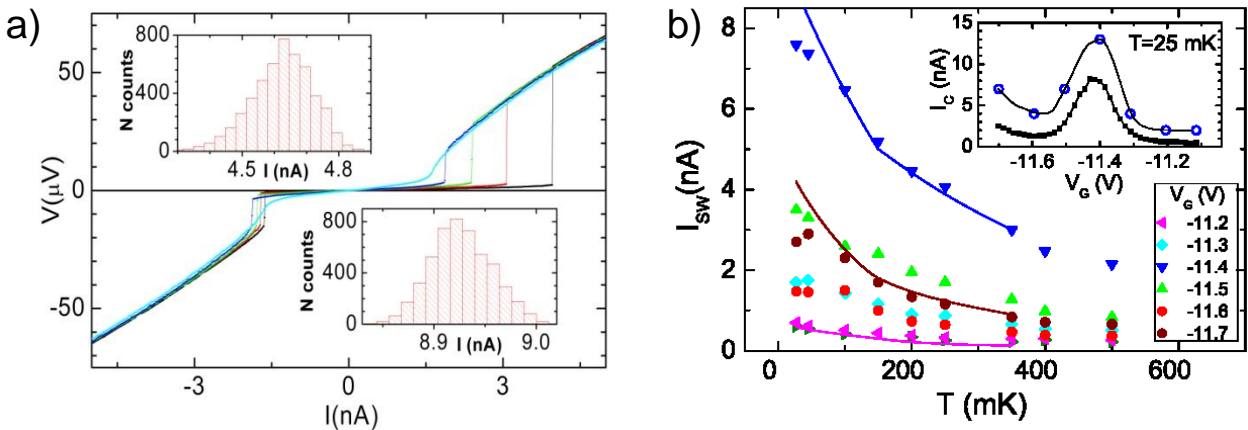


Figure 23: (a) IV -characteristics measured at $V_G = 22.3$ V. Different colours correspond to different temperatures, from 200 mK (highest switching current) to 600 mK (lowest switching current) in steps of 100 mK. The insets show two switching histograms with 5000 sweeps each, measured at $V_G = -22.3$ V, $T = 50$ mK (up left) and $V_G = -24.8$ V, $T = 150$ mK (down right). (b) Temperature dependence of the switching current for different gate voltages. The solid line is a fit to the data obtained from the thermal fluctuation theory. The inset shows the measured switching current together with the values of the intrinsic critical current I_C extracted from the fits.

For the physical interpretation of the data, it is important to note that observed temperature dependent switching current can be very different from the intrinsic $I_C(T)$ curve of the junction in absence of thermal fluctuations. Using a T -independent I_C as single fit parameter, we calculated

$I_{SW}(T)$ with the help of an extended resistively shunted junction RSJ-model containing thermal current noise and the coupling to an external RC circuit, which accounts for our on-chip electromagnetic environment. The solid lines in Figure 23b have been obtained using the measured junction resistance after the switch, the resistance of the external $R_{ext} = 350 \Omega$, and $C = 11.5$ pF the external capacitance. The capacitance of the Josephson junction is estimated as $C_J = 0.2$ fF, which can be neglected. The importance of fluctuations is quantified by the parameter $\gamma = 2ek_B T/I_C = 0.044 \cdot (T [\text{mK}])/(I_C [\text{nA}])$, where k_B is the Boltzmann constant. The crossover temperature T^* between the strong ($\gamma > 1$) and the weak ($\gamma < 1$) regime is determined by the condition $E_J(T) \sim k_B T^*$, where $E_J(T) = I_C(T)/2e$ is the Josephson coupling energy. It is thus clear that in our experiments, we operate the crossover region $\gamma \sim 1$. The agreement between the measured T dependence of the switching current I_{SW} with the model (solid line in Figure 23) is good, except at 100 mK, where the observed I_{SW} is slightly reduced. In the inset, we plot the switching current at 25 mK measured along the resonance and the corresponding critical currents extracted using the model described. We continued the experiments on CNT with Nb-leads, in order to further investigate the temperature dependence of the critical current in Nb/CNT/Nb-Josephson junctions. In voltage biased junctions, we find interesting fine structures in dV/dI at energies much smaller than those expected from multiple Andreev reflections, which so far are not understood (See 3rd Activity Report for further details).

4.3 Induced superconductivity in SWNTs (Task 4.2)

Kondo regime: We have fabricated Josephson quantum dot junctions by contacting a carbon nanotube with superconducting electrodes made from Ti/Al/Ti.³⁸ The Josephson Quantum dot junctions is in the Coulomb blockade regime (see Figure 24a) and intentionally designed to be overdamped in order to optimize the observable supercurrent. An observable supercurrent of up to 0.5 nA are seen in Figure 24b, where the differential resistance is plotted versus applied current and gate voltage. The dark regions correspond to a low resistance state of the nanotube where superconductivity is induced in the nanotube. The critical current of the junction is extracted by fitting the measured IV -curves to theory as shown in Figure 24c. The critical current is observed to oscillate from finite magnitude to zero and back to finite magnitude for every electron added to the QD (Figure 24d). This behavior is consistent with the so-called $0-\pi$ transition, where the critical current changes sign for every electron added to the QD.

³⁸ H. I. Jørgensen, T. Novotný, K. Grove-Rasmussen, K. Flensberg and P. E. Lindelof, *Critical Current 0-Pi Transition in Designed Josephson Quantum Dot Junctions*, Nano Lett. **7**, 2441 (2007).

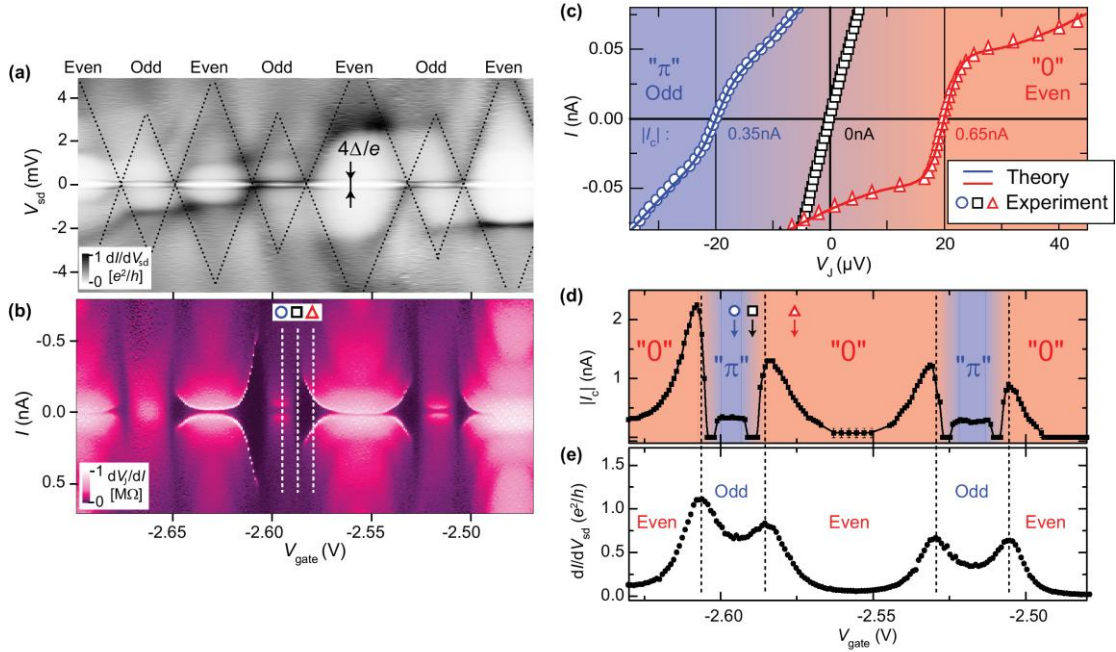


Figure 24: (a) Surface plot of the differential conductance (dI/dV_{sd}) versus bias voltage (V_{sd}) and gate voltage (V_G). Coulomb blockade diamonds, indicated with black dotted lines, are alternating in size between large and small with a corresponding even and odd number of electrons localized on the QD. (b) Surface plot of differential resistance (dV_j/dI) versus applied current (I) and V_G , in the same gate-voltage range as in (a). (c) Three $I-V_j$ curves from (b) at indicated positions, the right and left graphs are shifted by 20 μV for clarity. Circles are measured with odd occupation on the dot in the π junction regime, squares at the $0-\pi$ transition point, and triangles with even occupation on the dot in the 0 junction regime. The solid lines are fits to theory yielding critical currents of 0.65 nA (0.35 nA) for even (odd) electron occupation, and zero at the transition point. (d) Experimental critical current $|I_c|$ as extracted by fitting measured $I-V_j$ curves to theory, versus V_G . The error-bars in at the plateau around $V_G = -2.56$ V show the estimated precision of the fit. (e) Normal state differential conductance ($B = 150$ mT) at zero bias, in the same gate-voltage range as in (d). The dotted vertical lines indicate the positions of charge-degeneracy resonances.

From Kondo to Fabry-Pérot regime: In general, supercurrents are enhanced when going from Kondo to Fabry-Pérot regime even though the normal state conductance would be the same. This is illustrated by Figure 25 which displays the superconducting state IV curves in both Fabry-Pérot (FP) and Kondo regimes. As the sample is voltage biased, negative differential resistance (NDR) is observable in Fabry-Pérot regime. However, in Kondo regime, NDR occurs only at small measured critical current I_{CM} and it disappears around the maximum of the Kondo resonance peak where I_{CM} is large. We note that zero bias resistance and the IV -curves evolve smoothly with V_g around the Kondo resonance without any sudden jumps, and that $T_K > \Delta_g$. We ascribe the disappearance of NDR to the presence of large MAR- induced subgap current, which is stronger with respect to the supercurrent in the Kondo regime than in the FP case.

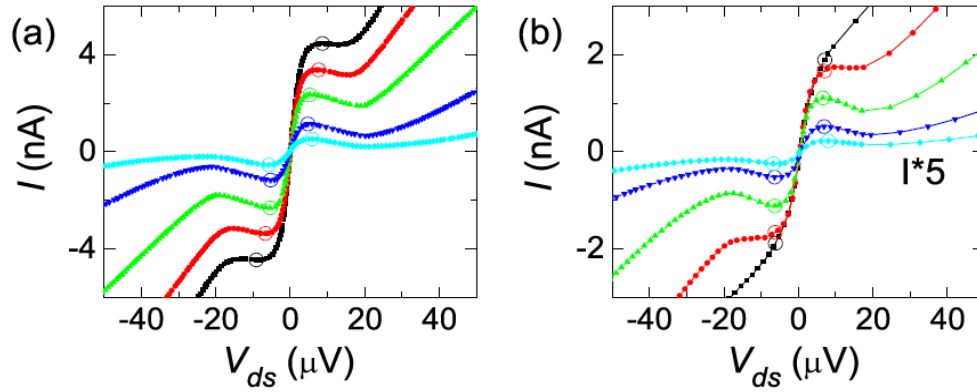


Figure 25: Superconducting IV -curves at a few gate voltage values in (a) Fabry-Pérot regime, and (b) Kondo regime. The circles with different colours show how the measured critical current I_{CM} was determined. Data in (a) were measured at $T = 60$ mK while data in (b) were taken from another cool-down at $T = 60$ mK with about the same value of normal state conductance as in (a).

In fact, our data display a wide distribution of Kondo temperatures $T_K = 1\text{--}14$ K (up to 10Δ), and the measured critical current I_{CM} vs. T_K displays two distinct branches; these branches, distinguished by zero-bias splitting of the normal-state Kondo conductance peak, differ by an order of magnitude at large values of T_K : resonances with zero-bias splitting, which appear in about every second of our Kondo peaks, result in a smaller critical current than for the regular Kondo maxima. For details, we refer to the 3rd Activity Report.

4.4 Induced supercurrents in graphene

Proximity-induced supercurrents up to 300 nA have been observed in graphene samples contacted using Al/Ti leads. Also, preliminary results on the current phase relation have been obtained. See Deliverable D27 for details.

4.5 Cooper-pair beam splitter using SWNTs (Task 4.3)

We applied the idea of crossed (or non-local) Andreev reflection (CAR) to carbon nanotubes. We have investigated three-terminal devices with two normal and one central superconducting contact we prepared, and investigated by low-temperature transport experiments. In our scheme, illustrated in Figure 26a, an electron injected into a SWNT via one normal (N) lead results in a Cooper pair in the superconducting (S) lead and a hole in the second N electrode. The corresponding time-reversed process is the splitting of Cooper pairs into two electrons, leaving through the two different N contacts. Hence, such a device (see the sample layout in Figure 26a) can be called a Cooper-pair beam splitter.

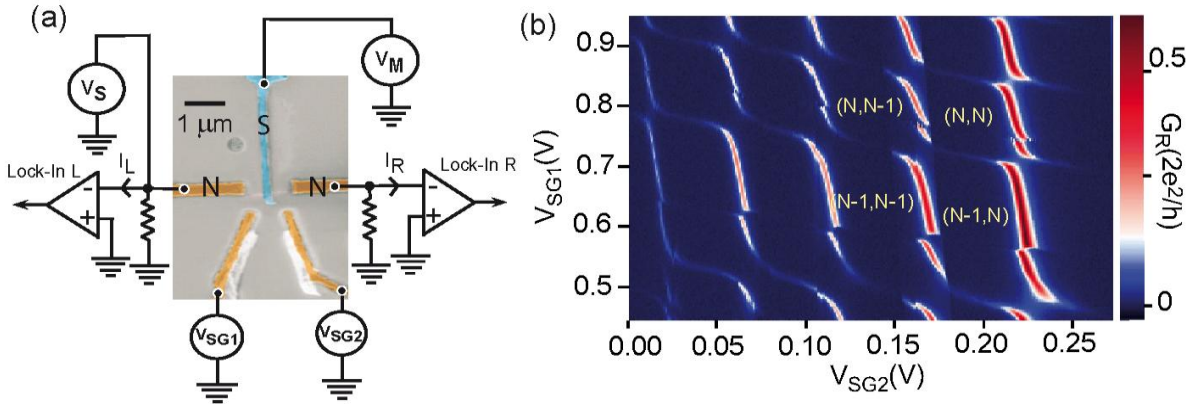


Figure 26: (a) SEM image of a Cooper-pair beam splitter device prepared by angle evaporation with measurement scheme. Two Pd contacts (orange) connect a SWNT. In addition, a central superconducting contact (blue) made from an Al/Pd bilayer serves as an injector for Cooper-pairs into the tube. (b) Stability diagram of the double dot with $40 \mu\text{V}$ bias voltage applied from source V_S . The yellow numbers indicate the charge states in neighbouring Coulomb valleys.

The very specific advantage of SWNTs for this purpose is that the deposition of three metallic electrodes onto a SWNT leads to the formation of a double quantum dot at low temperatures, as is demonstrated by the corresponding stability diagram in Figure 26b. The Coulomb repulsion between the two dots suppresses competing processes, where both electrons tunnel into the same dot. The experiment was performed in co-operation with the ENS group in Paris, where the measurements were performed by Lorenz Herrmann (on leave from Regensburg). The samples were prepared in Regensburg, based on our expertise with superconducting contacts to carbon nanotubes.³⁹ The characteristic curvature of the charging lines near the triple points in Figure 26b indicates that the tunnel coupling between the dots is rather strong. All normal state parameters of the sample are extracted from Figure 26b. The main result of our experiment is the observation of an enhanced current in the sub-gap bias regime, when injecting current via the S-contact into the nanotube. This sub-gap current results from a new type of co-tunneling event where the two partners of a Cooper-pair simultaneously tunnel onto the two dots, while all competing processes, like tunneling of two electrons into the same dot, are energetically unfavourable. At the triple points of the charging diagram, one additional electron can be placed without extra energy on each dot; a second electron on one of the dots requires an extra intra-dot charging energy. Thus, the latter process can occur only via a virtual intermediate state with an unpaired electron in the Al-finger.

The probability for such a second order process is much smaller than for a simultaneous transition of two electrons on the two dots, which requires no virtual states and is of first order in the ratio G_L/G_R in the normal state. Model calculations by A. Levy-Yeyati in Madrid show that local Andreev reflection (AR), where both electrons leave via the same contact, and crossed Andreev reflection (CAR) should depend in a different way on the ratio $\alpha_N = G_{LN}/G_{RN}$ of the normal state conductance of the two normal leads. The values for α_S and α_N are extracted from the conductance maxima at the triple points (see Figure 27a), which are taken along lines connecting a pair of triple points in the charging diagram (Figure 26b). For local AR the conductance ratio in the superconducting state $\alpha_S = G_{LS}/G_{RS}$ should be equal to α_N^2 , while for CAR one finds $\alpha_S = \alpha_N$. The fact that most of the data points lie on the straight green line in Figure 27b, means that a substantial amount of CAR takes place. In contrast, data taken far away from the triple points lie off the curved dashed line in Figure 27b. In this case one dot is Coulomb-blockaded and all electrons are forced to leave via the same lead. This corresponds to the case of local ARs. Our data thus strongly suggests the presence of crossed Andreev

³⁹ E. Pallecchi, M. Gaass, D. Ryndyk and Ch. Strunk, *Carbon Nanotube Quantum Dots with Nb Contacts*, Appl. Phys. Lett. **93**, 072501 (2008).

reflections, respectively the splitting of a significant fraction of the Cooper pairs impinging through the central electrode. Further details can be found in our submitted publication.⁴⁰

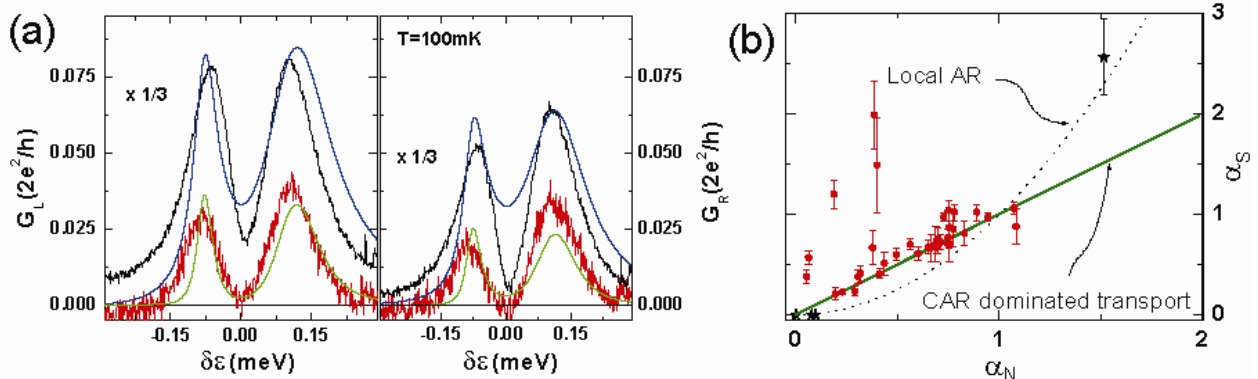


Figure 27: (a) Measured conductance through the left and right terminal, when biased at $40 \mu\text{V}$ (below the gap energy of the contact) through the superconducting injector contact at magnetic field $B = 0$ (S-state, red curve) and $B = 89 \text{ mT}$ (N-state, black curve). In the S-state the sub-gap current is still $\sim 20 \%$ of that in the N-state, indicating a substantial contribution of Andreev-reflection (AR) processes. The blue and green lines correspond to model calculations for the S and N cases. (b) Variation of the conductance ratio in the superconducting state $\alpha_S = G_{LS}/G_{RS}$ (red squares) versus the conductance ratio $\alpha_N = G_{LN}/G_{RN}$ in the normal state. The green solid line is the model prediction for crossed AR, the dashed results for local AR. The black stars were obtained aside from the triple points, where one of the dots is Coulomb blocked, which prohibits CAR and allows local AR only.

Our work is one of the first experimental realizations of a Cooper-pair beam splitter and opens new possibilities to investigate spin-entangled electrons and their application in quantum information processing. We envision experiments where the relative spin orientation of the emitted electrons by virtue of ferromagnetic contact electrodes is detected.⁴¹

4.6 High-frequency properties of nanotube junctions (Task 4.4)

Superconducting carbon nanotube devices provide mesoscopic components that are at the same time low-impedance and charge-sensitive. This is exceptional because typically the resistance of a nanosample has to be around the quantum resistance $R_Q = h/e^2$ in order to obtain charge quantization effects. The low-impedance nature of such devices makes them very attractive for high-frequency electrometry, as the matching circuits between samples and the 50Ω measuring setup can be avoided. In our work, we have investigated superconducting multi-walled carbon nanotubes (MWCNT) and determined their basic properties for such matching-free electrometers at 600–900 MHz frequencies. We have also employed nanotube Josephson junctions for non-hysteretic rf-SQUID operation as reported in Appendix I of D19. Deliverable D19 also discusses the background of the high frequency measurements with superconducting samples in comparison to regular rf-SET experiments.

The modulation of the reflection coefficient ($\partial|\Gamma|/\partial q_g = 1.5/e$, see D19) can be employed to estimate the sensitivity of the setup as an rf-electrometer. For a setup with a noise temperature of $T_N = 4 \text{ K}$, this implies a charge sensitivity of $4 \cdot 10^{-5} e/\text{Hz}^{1/2}$. This value compares quite well with the results obtained for regular rf-FETs (see Deliverable D13). According to our latest experiments, however, the phase diffusion cannot be described simply by dissipation in these measurements. The inductive component has to be taken into account, and further work is needed before the actual limit of sensitivity of these devices is known.

⁴⁰ L.G. Herrmann, F. Portier, P. Roche, A. Levy Yeyati, T. Kontos and Ch. Strunk, *Carbon Nanotubes as Cooper Pair Beam Splitters*, submitted to Phys. Rev. Lett., arXiv:0909.3243 (2009).

⁴¹ D. Preusche, S. Schmidmeier, E. Pallecchi, C. Dietrich, A. K. Huettel, J. Zweck and Ch. Strunk, *Characterisation of Ferromagnetic Contacts to Carbon Nanotubes*, accepted for J. Appl. Phys. (2009).

5 WP5 – Nanomechanical force sensor

5.1 Summary

In this workpackage, mechanical vibrations of suspended carbon nanotubes (and graphene) have been investigated. The main goal has been to develop nanotube resonators as inertial mass sensors. Specifically, the mass responsivity and the mass resolution were measured, two important parameters for the evaluation of the performance for mass sensing. The values for these quantities were found to be excellent; they surpass those reported previously for resonators made of nanotube or any other material. These results show that carbon nanotube is the material of choice for fabricating ultrasensitive mechanical resonators. The reason is that the mass of a nanotube is ultralow so that even a tiny amount of atoms deposited onto the nanotube makes up a significant fraction of the resonator's total mass. This result offers many new perspectives for mass spectrometry.

The main achievements reached in WP5 are (i) enhancement of nanotube resonator's Q-value up to 5100, (ii) an increase of the resonant frequency up to GHz range and mapping of the shape of the modes both in CNTs and graphene, (iii) a mass detection using a mechanical CNT resonator with a resolution of 1.7 zg at He temperature, and (iv) observation of coupling mechanical vibrations with charge transport.

5.2 Scanning force microscopy detection

The node in Barcelona has demonstrated a novel characterization method of nanotube resonator devices based on mechanical detection by scanning force microscopy (SFM). This method enables the detection of the resonance frequency in air at atmospheric pressure and the imaging of the mode-shape for the lowest bending eigenmodes. Fundamental eigenmodes of nanotubes were detected up to 3.1 GHz (Figure 28). The goal (ii) defined above was fulfilled and the results were published in Physical Review Letters and Nano Letters.

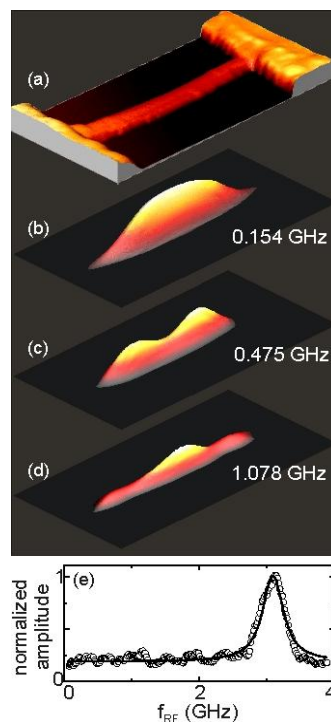


Figure 28: Mechanical resonances of MWNTs. Topography (a) and vibration images (b-d) are shown for a 770 nm long MWNT resonator. The length of the images is 1 μm and the width 0.5 μm . The vibration images have been low-pass filtered with identical parameters for the 3 images. (e) shows the resonance peak of the fundamental eigenmode for a 265 nm long MWNT resonator.

The nanotube motion is electrostatically actuated with an oscillating voltage applied on a gate electrode. As the driving frequency f_{RF} approaches the resonance frequency of the nanotube, the nanotube vibration becomes large. In addition, the amplitude of the resonator vibration is fully amplitude modulated at f_{mod} , which can be seen as sequentially turning on and off the vibration. The resulting envelope of the vibration amplitude is sensed by the SFM cantilever. Note that the SFM cantilever has a limited bandwidth response so that it cannot follow the rapid vibrations at f_{RF} .

In our experiments, the SFM is operated in non-contact mode to minimize forces applied on the nanotube by the SFM cantilever. The detection of the vibrations is optimised by matching the modulation frequency f_{mod} to the resonance frequency of the first eigenmode of the SFM cantilever, and by using an external lock-in amplifier tuned at f_{mod} . The second eigenmode of the SFM cantilever is used for topography imaging in order to suppress interferences in the detection of topography and vibrations. SFM cantilever eigenmodes are very weakly coupled and can be used as if they were different cantilevers to independently probe topography and sample vibrations.

5.3 Mass sensing

The node in Barcelona has used nanotube resonators as inertial mass sensors. Specifically, the mass responsivity and the mass resolution were measured, two important parameters for the evaluation of the performances for mass sensing. The values are excellent; they surpass those previously reported for resonators made of nanotube or any other material. These results show that carbon nanotubes are a material of choice to fabricate ultrasensitive mechanical resonators. The reason is that the mass of a nanotube is ultralow so even a tiny amount of atoms deposited onto the nanotube makes up a significant fraction of the total mass. This result offers many new perspectives for mass spectrometry. Because we realized that nanotube resonators have much more potential as mass sensors than force sensors, we focused on mass sensing. In addition, both sensing mechanisms are related. For these reasons, the reviewers of the project accepted this change in the goals of the project (goal iv). The results were published in Nano Letters at the same time as two other similar works from Berkeley and Caltech.

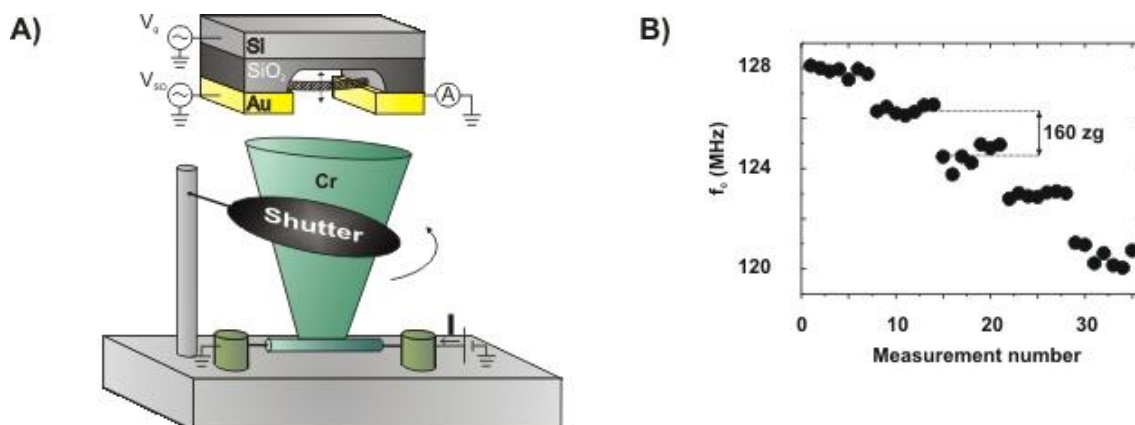


Figure 29: Mass sensing. (a) Schematic of the setup. Cr atoms are deposited onto the nanotube resonator in a Joule evaporator and the mass of the atoms adsorbed on the nanotube is measured. (b) Resonance frequency measured sequentially at 300 K. The resonance frequency shifts down stepwise each time 160 zg of Cr is evaporated onto the nanotube. The time between two points is 40 s except when Cr is evaporated (5 min).

The motion δz of the nanotube is detected via a capacitive technique. δz modulates the nanotube-gate capacitance, and, in turn, it modulates the charge in the nanotube. To track the high-frequency charge modulation, we employ a mixing technique.

Cr atoms are deposited onto the nanotube resonator by joule heating of a Cr bar in a metal evaporator. We choose Cr because it has a high binding energy on the nanotube wall. Figure 29 shows the shift in the mechanical resonance frequency each time 160 zg of Cr is deposited onto the nanotube. The mass resolution is obtained from the fluctuations of the resonance frequency. We achieve a mass resolution of 1.7 zg at liquid He temperature, which is better than the 7 zg that was measured before on microfabricated semiconducting resonators.

5.4 Coupling mechanical vibrations with charge transport

In a nanotube resonator, the nanotube mechanically vibrates and can in addition act as a transistor. That is, electrons flow through the nanotube from one electrode to the other one. The node in Barcelona found that the mechanical motion and the electrons are highly coupled. This coupling is very useful to harness the oscillating motion of the nanotube. In contrast to mechanical oscillators made of other materials, the dynamical motion of nanotubes can be widely tuned by an external electric means, which is very convenient for practical use. Specifically, the resonance frequency, the quality factor and the nonlinear dynamic of the motion can be modified by a large amount by sweeping a voltage on a nearby gate. By increasing the driving force, the dynamics becomes linear. Surprisingly, the measured the resonance splits in two peaks. One of the peaks can have a very high effective quality factor (up to 5100). The goal (i) defined above was fulfilled and the results were published in a Science paper at the same time as another similar work from Delft.

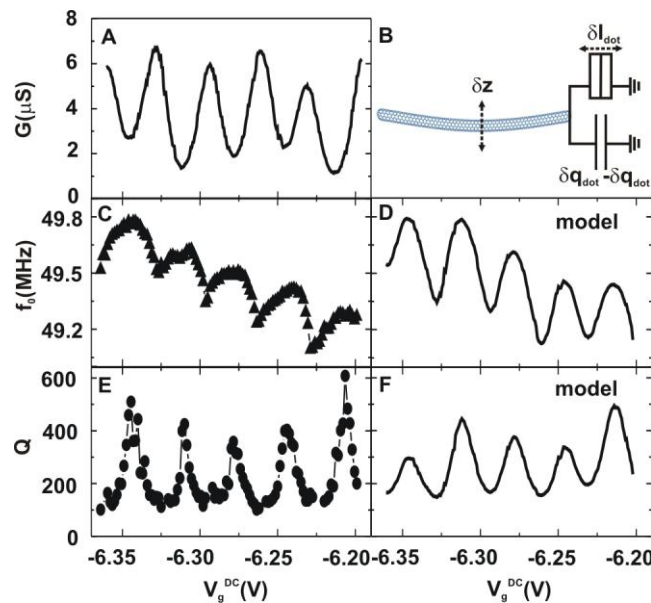


Figure 30: (a) Conductance of the nanotube as a function of the gate voltage at 4 K. (b) Schematic of the dissipation process. The mechanical oscillation charges and discharges the SWNT which results in a current flowing through the resistance at the nanotube-electrode interface. (c-d) Measured and calculated resonance frequency as a function of gate voltage. (e-f) Measured and calculated quality factor as a function of gate voltage.

Figure 30a shows the electron transport properties of the device; the SWNT differential conductance G at 4 K is plotted as a function of the constant voltage applied on the gate. G oscillates with the gate voltage in a way that is typical of the Coulomb-blockade regime. As for the mechanical properties, Figure 30c-d show a clear correlation with the electrical conductance. Indeed, G is the maximum, whereas the resonance frequency and the quality factor are low. This correlation suggests that the mechanical motion is influenced by Coulomb blockade.

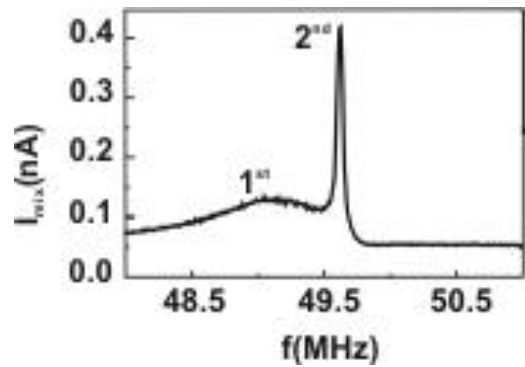


Figure 31: Nonlinear dynamic of the SWNT motion at 1.5 K. Mixing current as a function of driving frequency. A second peak appears that is very narrow.

We considered measurements in which the large driving force applied to the SWNT accesses the nonlinear dynamic of the motion. The resonance in Figure 31 has a surprising shape; it splits in two peaks, a broad and a narrow one. The most striking feature is that its width becomes narrower when increasing the driving force. The (effective) quality factor can increase up to about 5100.

5.5 High-bandwidth detection scheme

The nodes in Helsinki and Barcelona tried to detect the mechanical vibrations using a detection scheme with a high bandwidth. Namely, the motion is probed in a RF-SET detection scheme (goal (iii) defined above). RF-SETs based on a suspended nanotube were fabricated. Charge detection could be achieved, but the motion could not be probed.